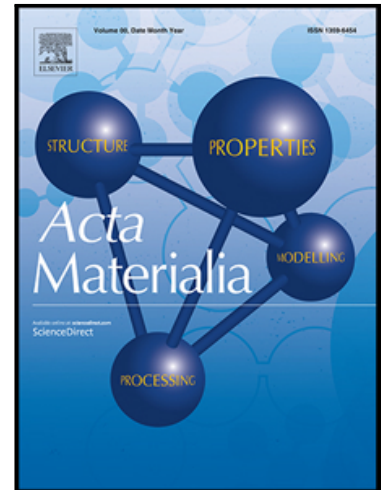# Journal Pre-proof

Rheological transitions in semi-solid alloys: in-situ imaging and LBM-DEM simulations

T.C. Su , C. O'Sullivan , H. Yasuda , C.M. Gourlay

Please cite this article as: T.C. Su , C. O'Sullivan , H. Yasuda , C.M. Gourlay , Rheological transitions in semi-solid alloys: in-situ imaging and LBM-DEM simulations, *Acta Materialia* (2020), doi: https://doi.org/10.1016/j.actamat.2020.03.011

Rheological transitions in semi-solid alloys: in-situ imaging and LBM-DEM simulations

Authors:

T.C. Su *,a, C. O'Sullivan [b], H. Yasuda [c], C.M. Gourlay [a]

Affiliations:

a. Department of Materials, Imperial College London, London, UK SW7 2AZ

b. Department of Civil and Environmental Engineering, Imperial College London, London,

UK SW7 2AZ

c. Department of Materials Science and Engineering, Kyoto University, Japan 606-8501

*Corresponding author:

E-mail of Corresponding author: t.su14@imperial.ac.uk

Abstract

Rheological transitions from suspension flow to granular deformation and shear cracking are investigated in equiaxed-globular semi-solid alloys by combining synchrotron radiography experiments with coupled lattice Boltzmann method, discrete element method (LBM-DEM) simulations. The experiments enabled a deformation mechanism map to be plotted as a function of solid fraction and shear rate, including a rate dependence for the transition from net-contraction to net-dilation, and for the initiation of shear cracking. The LBM-DEM simulations are in quantitative agreement with the experiments, both in terms of the strain fields in individual experiments and the deformation mechanism map from all experiments. The simulations are used to explore the factors affecting the shear rate dependence of the volumetric strain and transitions. The simulations further show that shear cracking is caused by a local liquid pressure drop due to unfed dilatancy, and the cracking location and its solid fraction and shear rate dependence were reproduced in the simulations

using a criterion that cracking occurs when the local liquid pressure drops below a critical

value.

Keywords：Semi-solid; Dilatancy; Synchrotron radiation; Image analysis; Discrete element

method

1. Introduction

Pressurised casting processes that deform alloys as they solidify are widely used.

Examples include high-pressure die casting [1-4], twin-roll casting [5-7], and the soft

reduction in the continuous casting of steel [8, 9]. However, their use is often limited by

semi-solid deformation-induced casting defects such as macrosegregation [6, 10-16], and

shear cracking [11, 17]. To optimize these processes and gain better control of these defects, a

deeper understanding of semi-solid alloy deformation is required.

Recent studies have proposed a granular mechanics framework [13, 18-22] for equiaxed

semi-solid rheology with similarities to critical state soil mechanics in civil engineering [23-

25]. A key feature of this framework is that the packing density (solid fraction) of the grains

changes during deformation, with grains pushing each other apart at high solid fraction

similar to Reynolds' dilatancy [26] in densely packed granular materials [24]. This

framework has been confirmed by direct observation of grain rearrangement during semi-

solid deformation using thin-sample radiography [27-34] and bulk-sample tomography [35-

37]. However, the combined influences of initial solid fraction and strain rate on semi-solid

deformation behaviour, cracking susceptibility, and interstitial liquid flow remain unclear.

A range of semi-solid modelling approaches have been developed including thixotropic

viscosity-based models [38-42], finite-element models describing the semi-solid as a

viscoplastic and partially cohesive medium [43-46], and thermomechanical model for studying deformation-induced macrosegregation [8, 47-52]. Some models have considered strain heterogeneity at the grain level either by coupling a hydromechanical granular model with the finite element method [53-56], including local grain rearrangement and a dilatancy term in a constitutive strain localisation criteria [57-60], or directly adapting the shape of equiaxed grains to generate a numerical assembly and using this in the particulate discrete element method (DEM) [61, 62].

A challenge in semi-solid deformation modelling is spanning across rheological transitions; for example, a model that can handle both the suspension regime and the granular regime (where grains/crystals form a percolating network), while capturing strain localization that can become casting defects. These challenges can be addressed by using DEM coupled with the lattice Boltzmann method (LBM), which can simulate interstitial liquid flow, solid-liquid interactions, and changes of local liquid pressure in response to dilation/contraction of the DEM grain assembly. DEM can be coupled with computational fluid dynamics (CFD). The main advantages of choosing LBM to couple with DEM are: (i) its ability to capture the interstitial liquid space without the need for remeshing, (ii) flexibility of specifying the spatial resolution and boundary conditions, (iii) the usage of a time-stepping algorithm which is similar to DEM, and (iv) a straightforward formulation of solid-liquid momentum interactions [63-69].

Previously, we presented a coupled LBM-DEM approach for simulating semi-solid alloy deformation and validated it against synchrotron imaging datasets of semi-solid shear [62]. Here, we extend the modelling approach to account for strain rate effects and demonstrate that it can capture the key features of synchrotron imaging experiments at shear rates spanning 10^{-4}–10^{-1}s^{-1} and solid fractions spanning 38% – 85%. The experiments and simulations are then combined to build the understanding of the rheological transitions that

occur with changing shear rate and solid fraction, and demonstrate that the modelling approach can span across these transitions.

2. Methods

2.1. Synchrotron radiography

Ingots of Al-xCu containing 6, 8, or 15 wt% Cu were cast with an Al-5Ti-1B grain refiner to create fine equiaxed microstructures. Thin-plate samples with thickness 150 - 200 µm and approximately one α-Al grain thick were prepared by slicing and grinding the ingots with SiC paper, and were then placed in the 200 µm thick cavity of the thin-sample direct-shear cell apparatus described in reference [30] and shown in Fig. 1a.

In-situ experiments were conducted on beamlines BL20XU and BL20B2 at the SPring-8 synchrotron using the in-situ heating, displacement and recording apparatus developed by Yasuda and co-workers [29, 70-73]. A monochromatic X-ray beam was used with energy of 14-16keV, and the transmitted beam was captured with a CMOS-detector after a phosphor screen [30, 74]. Depending on the beamtime, the square FOV had side length in the range 5.1 mm to 5.6 mm and was recorded as 1024x1024 or 2048x2048 images in 16-bit depth.

In each experiment, the whole deformation system was heated in the furnace to a temperature in the solid + liquid region under vacuum level < 10Pa. A constant mean volumetric solid fraction throughout the sample, g_S^0, with globular morphology was attained by isothermally holding the semi-solid sample for 30 minutes (^{0} indicates parameters prior to deformation). Note that some particles will be ground flat when preparing a 150 - 200 µm slice but, during isothermal holding in the semi-solid region for 30 minutes prior to deformation, these particles will become rounded again due to coarsening. Isothermal shear deformation was then applied by the upward displacement of a mobile 150 µm thick Al_2O_3

push plate with a nearly constant rate du_y/dt as indicated in Fig. 1a.

16 shear deformation experiments were conducted on semi-solid samples that had average grain size $\bar{d}$ less than 200 μm (with 500 – 2000 grains in the FOV), with a range of initial volumetric solid fractions between $g_S^0 = 44\% – 85\%$, and a range of constant push plate displacement rates from $du_y/dt = 1 – 2800$ μm·s^{-1} (corresponding to global shear rates on the order 10^{-4}–10^{-1}s^{-1}).

An additional heating experiment "38% - 0μm·s^{-1}" was conducted to explore the transition from a solid network to a floating suspension. An Al-15Cu sample with size 10mm × 5mm × 0.2mm was heated in the furnace to reach $g_S \sim 50\%$ and held for 30 minutes. The system was then heated stepwise with temperature increments of 2°C and held for ~ 30 seconds at each step. The X-ray imaging continued until the whole thin sample was totally remelted. Note that in the 38% - 0μm·s^{-1} dataset the push-plate was not moved and all grain motion occurred due to buoyancy.

2.2. Synchrotron image processing and quantification

The X-ray intensity processing followed the approach developed in references [27, 62] using an averaging approach on the fraction of solid in the beam path at each pixel based on the Beer-Lambert law [75]. The representative elementary volume (REV) was defined as a projected area of $\sqrt{10}\bar{d} \times \sqrt{10}\bar{d}$, where $\bar{d}$ is the mean α-Al grain size. The volumetric solid fraction prior to deformation g_S^0 was directly evaluated from the initial image for each dataset.

$$\frac{L_S^0}{L_{alloy}^0} = \frac{\ln I_{SL}^0 - \ln I_L^0}{\ln I_S^0 - \ln I_L^0} \qquad (1a)$$

$$g_{S.A}^0 = \left\langle L_S^0 / L_{alloy}^0 \right\rangle_A \qquad (1b)$$

where I_{SL}^0 is the intensity of the transmitted beam through the solid-liquid mixture, I_L^0 is the transmitted intensity through 100% liquid, and I_S^0 is the transmitted intensity through 100% solid. To measure the global g_S^0, the averaging area A was chosen to be close to the FOV.

The transmitted X-ray intensity through a sample during deformation, I_{SL}^n, is affected by small changes in the sample thickness field L_{alloy}^n in addition to the distribution of the solid and liquid phase (^{n} indicates parameters at frame n during deformation). L_{alloy}^n can be expressed as:

$$L_{alloy}^n = L_{alloy}^0 + \frac{\ln(I_{SL.min}^0/I_{SL.min}^n)}{\mu_L} + \frac{(\mu_L - \mu_S)(L_{S.min}^n - L_{S.min}^0)}{\mu_L} \qquad (2)$$

Eq. (2) is useful when the local minimum thickness of the solid phase $L_{S.min}^n$ can be evaluated (e.g., $L_{S.min}^n = L_{S.min}^0$ in a negligibly-deformed region, or $L_{S.min}^n = 0$ for any REV with a fully liquid region in the beam path). Alternatively, L_{alloy}^n can be evaluated from the transmitted intensity through regions of nearly 100% solid through Eq. (3):

$$L_{alloy}^n = \frac{\ln I_S^0 - \ln I_S^n}{\mu_S} + L_{alloy}^0 \qquad (3)$$

The volumetric solid fraction field for radiograph n, $g_{S.REV}^n$, was then obtained from the L_{alloy}^n and I_L^n fields:

$$I_L^n = I_L^0 e^{-\mu_L\left(L_{alloy}^n - L_{alloy}^0\right)} \qquad (4a)$$

$$g_{S.REV}^n = \left\langle \frac{L_S^n}{L_{alloy}^n} \right\rangle_{REV} = \left\langle \frac{\ln I_{SL}^n - \ln I_L^n}{L_{alloy}^n(\mu_L - \mu_S)} \right\rangle_{REV} \qquad (4b)$$

The REV-averaged solid fraction fields $g_{S.REV}^0$ and $g_{S.REV}^n$ were used to derive the volumetric strain field ε_{vol}^n caused by changes in solid packing density, giving the volumetric

strain of any REV:

$$\varepsilon_{vol}^n = \frac{g_{S.REV}^0}{g_{S.REV}^n} - 1 \tag{5}$$

2.3. Theoretical formulations for coupled LBM-DEM simulations

The simulations involved a coupled LBM-DEM approach in two-dimensions (2D) where the starting microstructures and boundary conditions were taken from thin-plate experiments. In this work, an LBM code was written in the *FISH* scripting language within the DEM program PFC2D Ver. 5.0 (Itasca Consulting Group, Inc). The coupled LBM-DEM approach is summarised in Fig. 2 and is explained in detail next.

The particulate discrete element method (DEM) reproduces a disordered grain assembly in contact (light grey particles in Fig. 1b and c), and models interactions between two DEM particles/grains by a specified mechanical contact model [76, 77]. Through updating positions and orientations of the DEM grains at discrete time intervals under dynamic equilibrium, the local changes in packing density due to grain rearrangement arise naturally as emergent phenomena. The lattice Boltzmann method (LBM) [78-83] was used to model the interstitial liquid (dark grey in the interstices in Fig. 1b and c). This method evaluates the evolution of the physical quantities of liquid flow by calculating the discrete Boltzmann equation across a discretised space (i.e. the regular blue grid in Fig. 1c and d).

In the DEM model, each globular α-Al grain is modelled as a pair of overlapping circles (Fig. 1c, and magnified view Fig. 1d) that interact with neighbouring grains through contact forces. For example in Fig. 1d, circle A1 (a sub-grain circle of grain A) and circle B2 (a sub-grain circle of grain B) are in contact. A finite amount of grain overlap (U_n in Fig. 1d) at this contact determines a contact force by a constitutive contact law; positions and orientations of grain A are updated from the average of contact forces and using an explicit Verlet type time

integration algorithm [84]. The constitutive contact law used in this paper is comprised of four components: (i) an elastic part, (ii) a damping part, (iii) a rolling resistance part, and (iv) a plastic force-displacement relationship. The first three parts are standard for DEM simulations on quasi-rigid particles. The fourth part was introduced to capture grain plasticity using the contact force-displacement relationship of an ideal plastic solid with very little work hardening [85] after a yielding contact force (effectively, the flow stress) F_y is reached, and including strain-rate sensitivity to the flow stress of the solid at $T/T_m{\sim}1$, similar to that previously measured in solid alloys at high homologous temperature [86]:

$$F_y - F_0 \approx 2.40 \times 10^{-8} \cdot \left[\frac{du_y}{dt}\right]^{0.26} \tag{6}$$

where F_0 is the average contact force magnitude prior to deformation. The coefficients for the contact model are summarized in Table 1, where k, μ, and μ_r were optimised and validated against in-situ semi-solid deformation experiments in reference [62] using the same shear cell and alloy. Greater detail of the constitutive contact law used is given in SI Section 2.

Fig. 1c and d show that both the DEM grain and interstitial space are covered by discretised regular lattice nodes, and each node (with position $\mathbf{x}_i$) accommodates fictive liquid that is allowed to move along 9 discretised directions ($\mathbf{e}_0 \ldots \mathbf{e}_8$, termed the LBM D2Q9 model [87]). The quantity of fictive liquid under equilibrium condition $f_\alpha^{eq} = f_\alpha^{eq}(\mathbf{x}_i, t)$ is:

$$f_\alpha^{eq} = w_\alpha \rho \left[1 + 3\frac{\mathbf{e}_\alpha \cdot \mathbf{u}}{c^2} + \frac{9}{2}\frac{(\mathbf{e}_\alpha \cdot \mathbf{u})^2}{c^4} - \frac{3}{2}\frac{\mathbf{u} \cdot \mathbf{u}}{c^2}\right] \tag{7}$$

where w_α is a weighting factor, $\rho = \rho(\mathbf{x}_i, t)$ is the macroscopic liquid density of the node $\mathbf{x}_i$, $\mathbf{u} = \mathbf{u}(\mathbf{x}_i, t)$ is the macroscopic liquid velocity vector, and c is the lattice speed defined as the ratio of the lattice node spacing δx (shown in Fig. 1d) to the LBM calculation timestep δt. The discretised velocities, $\mathbf{e}_\alpha$, and weighting factor, w_α, in the D2Q9 model can be

represented as [87]:

$$
\begin{aligned}
&\mathbf{e}_0 = c(0,0); w_0 = 4/9 \\
&\mathbf{e}_\alpha = c\left(\cos\left[\frac{(\alpha-1)\pi}{2}\right], \sin\left[\frac{(\alpha-1)\pi}{2}\right]\right); w_\alpha = \frac{1}{9} \quad \alpha = 1-4 \\
&\mathbf{e}_\alpha = \sqrt{2}c\left(\cos\left[\frac{(2\alpha-1)\pi}{4}\right], \sin\left[\frac{(2\alpha-1)\pi}{4}\right]\right); w_\alpha = \frac{1}{36} \quad \alpha = 5-8
\end{aligned} \tag{8}
$$

Non-equilibrium distribution functions $f_\alpha = f_\alpha(\mathbf{x}_i, t)$ for each node and the interaction between nodes are processed by collision and streaming schemes. The collision scheme operates within each node $\mathbf{x}_i$ locally to get updated distribution functions $f_\alpha(\mathbf{x}_i, t + \delta t)$. This research used an immersed boundary scheme (IBS) originated by Noble and Torczynski [64] to consider the moving obstacle (DEM grains) affecting the liquid flow:

$$
f_\alpha(\mathbf{x}_i, t + \delta t) = f_\alpha(\mathbf{x}_i, t) + B\Omega_\alpha^{Sjk} - \frac{1}{\tau}(1 - B)\left[f_\alpha(\mathbf{x}_i, t) - f_\alpha^{eq}(\mathbf{x}_i, t)\right] \tag{9}
$$

where τ is a dimensionless relaxation factor; $\tau = \lambda/\delta t$ (λ is relaxation time). Ω_α^{Sjk} refers to collision terms between circle k in grain j and liquid nodes associating with this circle shown in Fig. 1d. B is a weighting function expressed as:

$$
B = B(f_{S.xi}, \tau) = \frac{f_{S.xi}(\tau - 0.5)}{(1 - f_{S.xi}) + (\tau - 0.5)} \tag{10}
$$

$f_{S.xi}$ is the 2D solid fraction in the associated area [65] shown in Fig. 1d. The IBS evaluates the collision term Ω_α^{Sjk} based on the concept of "bounce-back" of the nonequilibrium part of the PDF [88]:

$$
\Omega_\alpha^{Sjk} = f_{-\alpha}(\mathbf{x}_i, t) - f_\alpha(\mathbf{x}_i, t) + f_\alpha^{eq}(\rho, \mathbf{u}_{Sjk}) - f_{-\alpha}^{eq}(\rho, \mathbf{u}) \tag{11}
$$

where $\mathbf{u}_{Sjk}$ is the velocity of the circle k in grain j. $-\alpha$ indicates the direction opposite to α.

For example, the opposite of f_7 is f_5. Note that this LBM-IBS framework has been widely used in ref. [65, 67, 89-92], and $B = 0$ will reduce Eq. (9) to typical LBM collision following the BGK model [93], which ensures mass and momentum conservation (equivalent to energy conservation for incompressible flows) [94]. The updated PDFs $f_\alpha(\mathbf{x}_i, t + \delta t)$ after the collision operation on each node should be streamed for the propagation of fluid packets to its neighbouring nodes $\mathbf{x}_i + \mathbf{e}_\alpha \delta x$:

$$f_\alpha(\mathbf{x}_i + \mathbf{e}_\alpha \delta t, t + \delta t) = f_\alpha(\mathbf{x}_i, t + \delta t) \tag{12}$$

Finally, the macroscopic liquid flow quantities (mainly liquid density $\rho = \rho(\mathbf{x}_i, t)$, momentum $\mathbf{j} = \mathbf{j}(\mathbf{x}_i, t)$, and flow velocity $\mathbf{u} = \mathbf{u}(\mathbf{x}_i, t)$) are updated based on the calculated non-equilibrium PDFs:

$$\rho(\mathbf{x}_i, t) = \sum_{\alpha=0}^{8} f_\alpha(\mathbf{x}_i, t) \tag{13a}$$

$$\mathbf{j}(\mathbf{x}_i, t) = \sum_{\alpha=0}^{8} f_\alpha(\mathbf{x}_i, t)\mathbf{e}_\alpha \tag{13b}$$

$$\mathbf{u}(\mathbf{x}_i, t) = \mathbf{j}(\mathbf{x}_i, t)/\rho(\mathbf{x}_i, t) \tag{13c}$$

The resulting momentum transfer $\Omega_\alpha^{Sjk}\mathbf{e}_\alpha$ in the bounce-back process (Eqs. (9) - (11)), together with momentum transfer calculated for the other circle in grain j, is used to compute the drag force $\mathbf{F}_j^d$ and moment M_j^d from all LBM liquid nodes ($1 \dots i$) acting on grain j with centroid $\mathbf{x}_{Sj}$:

$$\mathbf{F}_j^d = \frac{(\delta x)^2}{\delta t}\left(\sum_{k=1}^{2}\left[\sum_i B_i \sum_{\alpha=0}^{8} \Omega_\alpha^{Sjk}\mathbf{e}_\alpha\right]\right) \tag{14a}$$

$$M_j^d = \frac{(\delta x)^2}{\delta t}\left\{\sum_{k=1}^{2}\left[\sum_i (\mathbf{x}_i - \mathbf{x}_{Sj}) \times \left(B_i \sum_{\alpha=0}^{8} \Omega_\alpha^{Sjk}\mathbf{e}_\alpha\right)\right]\right\} \tag{14b}$$

It has been proven that the LBM collision and streaming schemes can simulate the fluid behaviour with kinematic viscosity ν (the ratio of dynamic viscosity μ to fluid density ρ) [69, 95, 96]:

$$\nu = \delta t \cdot c_s{}^2 \cdot (\tau - 0.5) \tag{15}$$

where $c_s = c/\sqrt{3}$ is the sound speed in the LBM domain. It should be noted that the LBM formulation is based on slightly compressible fluids at the incompressible limit [87] corresponding to low "computational" Mach number Ma defined as:

$$\text{Ma} = \frac{\max(|\mathbf{u}(\mathbf{x}_i, t)|)}{c_s} \tag{16}$$

He et al. [94] suggested that Ma should be lower than 0.1, which can be achieved by specifying τ in Eq. (15) to be close to 0.5. Finally, from the equation of state of an ideal gas, the fluid pressure field $p(\mathbf{x}_i, t)$ can be derived from the fluid density field:

$$p(\mathbf{x}_i, t) = \rho(\mathbf{x}_i, t) \cdot c_s{}^2 \tag{17}$$

Unlike real 3D materials, in 2D grain assemblies the solid and liquid phases cannot both form percolating networks at the same time. To address this difference, we follow past work on interstitial liquid flow and permeability in 2D simulations of packed granular materials and porous media [97-99], and used a hydrodynamic radius of $r_{hd} = 0.8$. Note that this reduced radius of solid obstacles was applied only in the LBM steps (e.g. circle C1 in Fig. 1d), and the full particle radius was used in all the DEM steps.

2.4. Computational procedure

Polydisperse two-circle grains were generated in PFC2D by inputting 20 grain templates, which were defined by measuring the grain size and shape distribution of a real thin-plate experiments. These grains with initial $k_n = 1 \times 10^4 \, \text{N} \cdot \text{m}^{-1}$ were isotropically compressed by a rectangular box, whose size was the same as the experiment. A servo-controlled mechanism was applied during isotropic compression until the four side walls reached a target 2D stress of $500 \, \text{N} \cdot \text{m}^{-1}$.

Since thin-plate semi-solid samples were constrained by surface tension at the free surfaces rather than by reaction forces from the outside Al_2O_3 walls, a moveable membrane boundary similar to ref. [62, 100, 101] was created to replace the four walls. This membrane boundary (red grains in Fig. 1b) was comprised of parallel-bonded grains, and each surface grain received a constraint force, $\mathbf{F_N}$, with direction inward to the assembly if the length of grain displacement outward was higher than 50 μm. Creation of a DEM grain assembly was completed when a DEM calculation cycle reached 2×10^6 and all grain velocities were less than $10^{-7} \, \text{m} \cdot \text{s}^{-1}$. Different initial 2D packing fractions were then generated from this sample. Lower initial solid fractions were created by slightly reducing the radius of all grains and/or by deleting some grains. Higher initial solid fractions were created by slightly increasing the radius of all grains and/or by adding smaller grains into some interstices.

The mass density of DEM grains, ρ_S, in Table 1 was slightly adjusted for samples with different $f_{S.pk}^0$ to account for the changes in α-Al composition and temperature at different solid fraction using equations from ref. [102], but the simulated results would not be significantly altered if a single density had been used. Table 2 summarises the coupled LBM-DEM simulations included in this paper. All boundary conditions were selected to be as close to the individual experiments as possible, based on direct in-situ imaging of the loading geometry and microstructure, and taking account of the fact that the samples never made

contact with the Al_2O_3 bounding walls for the small push-plate displacements $(10\bar{d})$ modelled here.

In 'step 1'of the flow diagram (Fig. 2), the DEM grain assembly with DEM cycle number $n_0 = 2.5 \times 10^6$ was obtained. All samples were covered by LBM nodes with spacing 40 μm in 'step 2', and the LBM grid was larger than whole DEM sample to accommodate the deformation of the DEM membrane without the need to re-define the grid.

The key LBM parameters (listed in Table 3) were defined in 'step 2': liquid density, ρ_L, in correspondence to ρ_S and calculated from ref. [102], dynamic viscosity, μ_L, from ref. [103], and LBM liquid calculation timestep, δt, which was specified to ensure calculation efficiency and low computational Mach number (Eq. (16)). After selecting a suitable Δt (in Table 1) and δt (in Table 3), an integer parameter "LBM-DEM timestep ratio", $r_{\delta t/\Delta t} = \delta t/\Delta t$, naturally evolves to explicitly define the number of DEM cycles required before implementing an LBM cycle, as listed in Table 3.

Adjustment of ρ_L and μ_L relating to different $\bar{d}$ and $f_{S.pk}^0$ among simulations gave the liquid kinematical viscosity $\nu = \mu_L/\rho_L$ in the narrow range 5.72-6.75×10^{-7} m^2·s^{-1}, showing the increase of solute concentration in the liquid with the rise of $\bar{d}$ and $f_{S.pk}^0$ does not have a significant effect on liquid flow. The weighting function B for the LBM collision process was evaluated using Eq. (9) in 'step 3', and all nodes were initialised to have liquid density ρ_L (Table 3), zero flow velocity, and $f_\alpha = f_\alpha^{eq}$ in 'step 4'.

A DEM calculation cycle was then implemented corresponding to steps 5 – 8 in Fig. 2. Note that in 'step 7', gravity was not included in all shear deformation simulations as the movement of grains in the experiment is observed to be majorly controlled by physical contacts. 'Step 9' checked if the DEM dynamic calculation has been implemented $r_{\delta t/\Delta t}$ times. If so, a LBM calculation cycle is implemented corresponding to steps 10 – 17 in Fig. 2. The momentum transfer at a solid-liquid interface is solved in this two-way coupled LBM-

DEM model since the velocities of DEM grains ('step 8') influence the LBM collision process ('step 13') by including the collision term Ω_α^{Sjk} in Eq. (9), while the drag force and moment of the LBM liquid ('step 17') acting on the DEM grains (Eq. (14)) are included in the calculations of accelerations of DEM grains ('step 7').

In 'step 15', all LBM boundary nodes were specifically treated to adapt to the changing shape of the DEM assembly: the LBM nodes outside of the DEM membrane boundary or overlapping with the push-plate were identified as an effective "solid zone" to inhibit liquid Al from flowing out of the DEM sample. When the DEM sample deforms, the LBM solid zone is adapted from the new shape of the membrane and the position of push-plate. A simulation was complete when the push-plate displacement u_y reached $10\bar{d}$ as checked in 'step 18'.

To simulate the heating experiment and the transition from a solid network to a floating suspension, a Float - 0µm·s⁻¹ sample was created using grain shapes and specimen size (10.0 mm × 5.0 mm) from the 44% - 30µm·s⁻¹ and 38% - 0µm·s⁻¹ datasets. A DEM grain assembly with $f_{S.pk}^0 \approx 78\%$ was created, and LBM-DEM calculation cycles (Fig. 2) were applied. To simulate the partial melting of solid grains, before the LBM grid covering the DEM assembly was applied ('step 2' in Fig. 2), the area of each two-circle grain was reduced by 10%. During the DEM simulation of grain floating, all grains were influenced by a buoyancy field $(1 - \rho_L/\rho_S)\mathbf{g}$ in 'step 7' to simulate floating suspension behaviour under non-percolating conditions. The simulation stopped when the velocity magnitude of all grains was less than 10^{-7} m · s⁻¹ (i.e., a stable percolating assembly reformed). The procedure was then repeated to simulate the heating experiment, whereby the area of each two-circle grain was further reduced by 10% to remove all force-transmitting contacts. The LBM liquid was re-initialised through steps 3 and 4 in Fig. 2. Additional dynamic calculations were implemented to reform a loosely packed assembly again under the buoyancy field.

2.5. Post-simulation analysis

The total volumetric strain of the sample, $\varepsilon_{vol}^{\text{DEM}}$, at a given time was calculated from the area of the sample prior to deformation A_0, and the current area, A_{def}.

$$\varepsilon_{vol}^{\text{DEM}} = \ln\left(\frac{A_{def}}{A_0}\right) \tag{18}$$

A_{def} was obtained from the area of the polygon joining the centroids of all membrane grains minus the push-plate penetration area.

The heterogeneous strain field was evaluated through a continuum-based triangulation approach [104-106] which outputs strain components ε_{xx}, ε_{yy}, and γ_{xy} [104]. The volumetric strain for each element was defined as $\varepsilon_{xx} + \varepsilon_{yy}$, and the shear strain ε_{xy} was approximated as $0.5\gamma_{xy}$. These strain fields were further smoothed using a $\sqrt{10}\bar{d} \times \sqrt{10}\bar{d}$ average filter.

The change of liquid pressure $\Delta p(\mathbf{x}_i, t)$ at each LBM node was derived from the change of liquid density for each LBM node $\rho(\mathbf{x}_i, t)$ by re-writing Eq. (17).

$$\Delta p(\mathbf{x}_i, t) = (\rho(\mathbf{x}_i, t) - \rho_0)c_s^2 \tag{19}$$

3. Results and Discussion

3.1. Semi-solid deformation map from the radiographic datasets

In all 17 X-ray imaging experiments spanning solid fractions from 38% – 85% and displacement rates from 1 – 2870 µm·s^{-1} (approximately = 10^{-4} – 10^{-1} s^{-1} strain rate for homogeneous shear), the semi-solid deformation behaviour could be classified into one of four categories: floating suspension, shear-induced contraction, shear-induced dilation, and shear cracking. Typical examples are shown in Fig. 3. Each deformation behaviour can be defined as follows:

1. Suspension: the solid fraction is lower than a critical value, such that the grain assembly does not form a percolating network. In the absence of forced convection, if the solid and liquid have different densities, the solid packs itself via grain settling/buoyancy without external loading.

2. Shear-induced contraction: within a percolating solid network, shear deformation pushes grains closer together leading to a reduction of total interstitial space (Fig. 3a and d). Liquid is expelled.

3. Shear-induced dilation: within a percolating solid network, shear deformation causes initially tightly-packed grains to push one another apart leading to expansion of the interstitial spaces (Fig. 3b, e, and Fig. 4). Liquid is drawn in.

4. Shear cracking: the generation of cracks during shear where the remaining liquid phase fails to flow into the expanding interstices (Fig. 3c and f). This often occurs by a meniscus being drawn into the liquid between grains in response to a decreasing liquid pressure.

The contraction or expansion of liquid interstices corresponds to volumetric strains in the grain assembly, which are quantified using Eq. (5) to plot volumetric strain maps ε_{vol}^{n} in Fig. 3g-i. The ε_{vol}^{n} field for the shear-induced contraction dataset in Fig. 3g is mostly

contractive (blue) ahead of the push plate, while for the shear-induced dilation dataset in Fig. 3h, there is a small compaction zone (blue) and a large zone undergoing shear-induced dilation (red). This dilating region corresponds to expanding liquid interstices as shown in more detail in Fig. 4, where the liquid is more attenuating and appears black and the grains (grey) can be seen to become less tightly packed during (isothermal) deformation.

Fig. 3i shows the ε_{vol}^n map of a radiograph before shear cracking has started at $u_y = 3.9\bar{d}$ (which is a much smaller push-plate displacement than Fig. 3f which is after severe cracking has developed). Fig. 3i shows a narrow band of positive volumetric strain approximately parallel to the parting plane due to localised shear-induced dilation.

Note that the negative ε_{vol}^n regions (blue) to the bottom-right of the FOV in Fig. 3h, and the top-right of the FOV in Fig. 3i represent local contraction due to the liquid being sucked away to the dilating regions in the sample. This liquid flow phenomenon results in an increase in transmitted X-ray intensity as can be seen in the bottom-right of the FOV in Fig. 3e and 4.

Fig. 3j is a map of deformation behaviour using g_S^0 as the horizontal axis, du_y/dt as the vertical axis, and indicating the deformation behaviour by different colours. Each datapoint represents one radiography dataset. The initial void ratio e^0 on the top axis has been converted from g_S^0 using the relationship $e^0 = (1 - g_S^0)/g_S^0$, and the shear rate on the right axis is evaluated from dividing du_y/dt by the sample width. Note that, within a net dilative (green) or contractive (black) sample, there was often both local dilation and local contraction and the deformation map plots the net behaviour. The transitions between different behaviours are shown qualitatively by drawing boundary lines on the deformation map. In Fig. 3j, the vertical $g_S^0 = 38\%$ line is the suspension-to-percolating-network transition obtained from the 38% - 0μm·s^{-1} dataset. The transition from shear-induced contraction to dilation line is inclined such that higher du_y/dt encourages dilation. The transition to shear-

cracking is strongly rate-dependent, occurring at lower solid fraction at higher du_y/dt. These transitions are explored in turn in the remainder of this paper.

3.2. The transition from a suspension to a percolating assembly

The suspension behaviour of the sample in the stepwise heating X-ray experiment is illustrated in Fig. 5a-d. In Fig. 5a, $g_S^0 \approx 38\%$ was measured on a radiograph just before the onset of grain floating using the FOV as the averaging area. During stepwise heating, the solid fraction decreased, the percolating network was lost and grains became buoyant and floated until they packed into a new solid network with neighbouring grains at the top of the sample, leaving a fully liquid region at the bottom. This can be seen in Fig. 5b and c. To study the packing density of the solid network created by floating grains, the region of the packed area was defined as the region, $A = PK$, in which all grains had displacement < 2 μm within the previous 10 seconds. The solid fraction in this region, $g_{S.PK}^n$, was measured as indicated in Fig. 5b and c. 20 pairs of $g_{S.FOV}^n$ and $g_{S.PK}^n$ were measured from radiographs during remelting and are plotted in Fig. 5d against the experiment time after the grains first became buoyant. It can be seen that the solid fraction of the packed layer remains near-constant as the overall solid fraction decreases, with $g_{S.PK}^n = 37\% \pm 1\%$, which is close to the $g_S^0 \approx 38\%$ when grains first became buoyant. Thus, for the globular grain morphology studied here, 38% is the approximate percolation threshold for a solid network. This is related to the dendrite coherency point measured in previous work which marks the onset of resistance to shear and compressive deformation [107, 108]. The coherency point is known to be strongly dependent on the crystal shape, ranging from ~10% for highly branched dendrites with a high liquid fraction within dendrite envelopes [108] to ~55% for fully-globular crystals [107, 108]. With consideration of the non-spherical grain shape, the 38% percolation threshold measured is comparable to the onset of measurable shear resistance of irregular globular microstructures

from past studies [109-111].

The onset of floating in the heating experiment (Fig. 5a-d) was explored by a LBM-DEM suspension simulation, as shown in Fig. 5e-h. The initial microstructure shown in Fig. 5e represents DEM grains after 10% reduction of the area of each two-circle grain so that the percolating network is lost and the grains can move under the buoyancy field. During the floating simulation where all DEM grains are under a buoyancy field $(1 - \rho_L/\rho_S)\mathbf{g}$, a liquid flow pattern was created by the drag of many DEM grains on the liquid (Fig. 5f). A percolating assembly then formed naturally within the simulation with a packing fraction $f^n_{S.pk.PK} \approx 77\%$ (Fig. 5g).

After measuring $f^n_{S.pk.PK} \approx 77\%$ at $t_{\mathrm{DEM}} = 20.0$ seconds (Fig. 5h), the overall packing fraction $f^n_{S.pk.FOV}$ was changed to 64% by a further 10% area reduction of grains, and a percolating assembly with $f^n_{S.pk.PK} \approx 76\%$ formed by $t_{\mathrm{DEM}} = 40.0$ seconds (Fig. 5h). Five pairs of $f^n_{S.pk.FOV}$ and $f^n_{S.pk.PK}$ in the packed zone are plotted in Fig. 5h and suggest a 2D percolation limit $f^n_{S.pk.PK} \approx 77\%$ in the loosely packed assembly comprised of two-circle grains. This result is similar to the random loose packing fraction ($\approx 77\%$) of simulated 2D frictional bidisperse discs in past work [112, 113].

Note that packing in 2D is more efficient than in 3D. For example, (i) hexagonal ordered close packing of uniform discs/spheres have packing fraction of 91% in 2D [113] and a face centred cubic packing has a packing fraction of 74% in 3D [113]; (ii) disordered loose packing of polydisperse discs/spheres have a packing fraction of $\approx 77\%$ in 2D [112] and $\approx 54\%$ in 3D [114]; and (iii) the packing fraction for uniform perfect disks on a square lattice is 79%, while the packing fraction for a single layer of perfect spheres on a square lattice is 52% (The simulations consider 2D disk clusters, while the single layer of spheres is analogous to the thin layer of crystals considered in the experiments here). The grain shape is also known to have a strong influence on the packing fraction [61, 115, 116]. Therefore, the difference

between the 2D simulated packing fraction of 77% and the 3D experimental packing fraction of ~38% is due to both 2D vs 3D effects and the more complex and irregular shape of the real grains.

A large body of past work on the rheology of metallic suspensions has involved strong forced convection [117-119] where settling/floating does not occur. This study shows that, without forced convection and given enough time, the semi-solid suspension floats (inverse settling) into a packed layer with solid fraction close to the percolation limit, and that the LBM-DEM approach is well-suited to modelling this behaviour.

3.3. The transition from net contraction to net dilation

For samples containing a percolating grain network, the transition from shear-induced contraction to shear-induced dilation is the boundary between green and black datasets in Fig. 3j. This transition was studied at constant displacement rate in our previous work [62] using four of the datasets in Fig. 3j (44% 50%, 66%, 71% solid at $30\mu m \cdot s^{-1}$) with our previous rate insensitive LBM-DEM model [62]. It was shown in ref. [62] that the simulations and experiments were in good quantitative agreement. Grains in the low solid fraction alloys (44% and 50% solid) were pushed closer together during deformation, resulting in a solid fraction increase and net-contraction. Grains in the high solid fraction alloys (66% and 71% solid), on the other hand, pushed one another apart during grain rearrangement under the action of compressive and shear contact forces, causing solid fraction decrease and net-dilation.

Fig. 3j also contains a net contraction-dilation transition at constant initial solid fraction with increasing shear rate (the 50% solid datasets at $30\mu m \cdot s^{-1}$, $1310\mu m \cdot s^{-1}$ and $2870\mu m \cdot s^{-1}$). These datasets were compared quantitatively with the new rate sensitive LBM-DEM model after digitising the initial microstructures and sample geometries from the $g_S^0 = 50\%$

experiments. Here, the comparison between the localised ε_{vol}^n field from the experiments (Fig. 6a) and the $\varepsilon_{xx} + \varepsilon_{yy}$ field from simulations (Fig. 6b) is simplified by the conversion from two-dimensional strain fields to averaged one-dimensional line profiles by averaging along x or y within a ROI. In Fig. 6c, e, and g (plots with red axes), the solid lines correspond to experimental ε_{vol}^n measurements and the dash-dot lines correspond to LBM-DEM simulated $\varepsilon_{xx} + \varepsilon_{yy}$ taken from the red ROI (box outlined by the red-dahsed line in Fig. 6a and b, which is averaged along y). The red ROI was selected to investigate the development of heterogeneous volumetric strain across the parting plane. Fig. 6d, f, and h (plots with blue axes), correspond to the blue ROI ahead of the push-plate (box outlined by blue-dashed line in Fig. 6a and b, which is averaged along x). The blue ROI was selected to investigate the transitions of contraction-to-dilation response ahead of the push plate. A detailed description on the definition of ROI positions and averaging on strain maps are in SI Section 3.

As shown in Fig. 6c-h, there is good agreement between experiments and simulations. Both the 50% - 30μm·s⁻¹ experiment and simulation I (Fig. 6c and d) show net-contraction in front of the push plate, and negative volumetric strain to $y \approx 12\bar{d}$ in the blue ROI (Fig. 6d) and at $x < 3\bar{d}$ in the red ROI (Fig. 6c) is captured. For deformation at higher du_y/dt of 1310μm·s⁻¹ shown in (Fig. 6e and f), the volumetric strain profiles in the 50% - 1310μm·s⁻¹ experiment and simulation II are still net-contractive, but the volumetric strain ahead of the push plate is notably less negative than Fig. 6c and d. There are two locally dilative zones with peaks at $x \approx 0$ and $x \approx 8\bar{d}$ in Fig. 6e, which are due to the complex heterogeneous liquid flow phenomena during the deformation experiment. Fig. 6g and h show that deformation at the higher push-plate displacement rate of 2870μm·s⁻¹ gives rise to a net-dilative response with a distinctive zone of positive volumetric strain ($-1.5\bar{d} < x < 6.5\bar{d}$ or $7.5\bar{d} < y < 22.5\bar{d}$ with a nearly 0.2 volumetric strain peak) and a slight contraction field near the push plate front. Simulation III also captures another negative volumetric strain

region to the right of the red ROI (Fig. 6g) starting at $x \approx 6.5\bar{d}$ in the 50% - 2870μm·s⁻¹ experiment due to the liquid being drawn away to feed dilation near the parting-plane. A similar phenomenon is observed at $y > 17.5\bar{d}$ in the 50% - 1310μm·s⁻¹ experiment and simulation II (Fig. 6f).

A key result in Fig. 6 is that, in addition to important features in the volumetric strain field, the simulations also correctly reproduce the transition from net contractive deformation (at 30 and 1310μm·s⁻¹) to net dilative deformation (at 2870μm·s⁻¹) when the displacement rate increases keeping the initial solid fraction constant. While the simulations are 2D, the thin-sample experiments can be considered to be 2.5D thick with interactions from the confining walls. The quantitative agreement between the experiments and simulations is because only a small change of sample thickness of <0.1$\bar{d}$ occurred in the experiments which makes the assumption of in-plane deformation reasonable. In future, it will be valuable to perform time-resolved 3D tomography experiments coupled with 3D LBM-DEM simulations.

It is then of interest to study the rheological transition from shear-induced contraction to shear-induced dilation in a matrix of simulations using the same starting geometry to remove any effects due to differences in the starting microstructure. Fig. 7 shows simulated deformation microstructures for the 4×3 matrix of solid fractions and shear rates, where the starting microstructure was the same at each shear rate. Some localisation phenomena can be seen across this matrix. First, the light-grey regions immediately ahead of push-plate in Fig. 7 correspond to a reduction of the mean distance between adjacent grains partly due to viscoplastic deformation of the solid phase ahead of the Al_2O_3 push-plate (similar to the experiments, e.g. Fig. 3d-e and Fig. 4). The simulations with a higher displacement rate have a smaller compacted zone at the push-plate front, and the dark-grey liquid interstices in Fig. 7 tend to localise along the parting plane when both $f_{S.pk}^0$ and du_y/dt are high especially for

the 93%PK - 2150μm·s^{-1} and 95%PK - 2150μm·s^{-1} simulations.

The simulated volumetric strain field, $\varepsilon_{xx} + \varepsilon_{yy}$, and the total volumetric strain, ε_{vol}^{DEM}, for each LBM-DEM simulation in the same 4×3 matrix are shown in Fig. 8. A transition from net contraction (black) to net dilation (green) can be seen in the simulations which follows a similar trend to the "inclined" contraction-to-dilation transition in the shear deformation experiments (the black-green line in Fig. 3j).

For the volumetric strain field $\varepsilon_{xx} + \varepsilon_{yy}$ in Fig. 8, increases in $f_{S.pk}^{0}$ and du_y/dt generally encourage dilation and reduce the contractive zone ahead of the push-plate. For example, among the four $\varepsilon_{vol}^{DEM} < 0$ (black) simulations with high compaction on an initially loose assembly and viscoplastic deformation of the solid phase ahead of the push-plate, there are some pockets of local dilation along the parting plane in the 81%PK - 2150μm·s^{-1} and 84%PK - 1μm·s^{-1} simulations. The other eight $\varepsilon_{vol}^{DEM} > 0$ (green) simulations develop a dilation zone from the parting plane to the left side of the FOV farther from the push-plate. The 93%PK - 2150μm·s^{-1} and 95%PK - 2150μm·s^{-1} simulations even show dilation immediately ahead of push-plate because grains still push each other apart after grain-level viscoplastic deformation. These net-dilation simulations also contain some local contraction regions in the right side of the FOV where liquid is drawn away to feed dilating interstices in the red regions. This phenomenon is also found in the shear deformation experiments (e.g., the blue region in Fig. 3h).

Fig. 9 shows simulated shear strain fields ε_{xy} from triangulation on the same 4x3 matrix. A positive ε_{xy} (red) region is generally localised above the top-right corner of the push plate across the whole 4×3 matrix of simulations. The formation of negative ε_{xy} (blue) regions near to the left boundary of the FOV is due to the left parting plane above the top-left corner of push-plate.

The change in the liquid pressure $\Delta p(\mathbf{x}_i, t)$ in response to shear deformation is shown in

Fig. 10. Interstitial liquid that is red has a positive change in pressure, blue has a negative change in pressure, and yellow has a pressure drop that exceeds a critical negative value (of -0.03 Pa that will be explained and discussed in the final section of the paper). Comparison of the liquid pressure change fields in Fig. 10 with the volumetric strain in Fig. 7, gives insights into the coupling between the changing packing density of the solid, liquid flow and the change in interstitial liquid pressure. The datasets with net-positive change in liquid pressure (red) in Fig. 10 have net contractive volumetric strains ($\varepsilon_{vol}^{\text{DEM}} < 0$) in Fig. 8. Conversely, datasets with net-negative change in liquid pressure (blue) in Fig. 10 have net dilative volumetric strains ($\varepsilon_{vol}^{\text{DEM}} > 0$) in Fig. 8. However, the liquid pressure field $\Delta p(\mathbf{x}_i, t)$ does not simply mirror the local volumetric strain ($\varepsilon_{xx} + \varepsilon_{yy}$) field. This is mainly because, in addition to the volume change of the liquid interstices, both the permeability of the grain assembly and the dissipation of excess liquid pressure contribute to the evolution of the $\Delta p(\mathbf{x}_i, t)$ field. For example, the $1\mu\text{m}\cdot\text{s}^{-1}$ simulations have sufficient time (more than 1000s to reach $10\bar{d}$ deformation) to dissipate the change of liquid pressure, resulting in nearly uniform $\Delta p(\mathbf{x}_i, t)$ fields, and 81%PK simulations have higher permeability for liquid flowing between the grains. The dissipation of excess liquid pressure becomes limited in high $f_{S.pk}^0$ and du_y/dt simulations.

3.4. Understanding the strain rate dependence of the contraction/dilation transition

The strain rate sensitivity has three main components: (i) the strain rate sensitivity of the plastic flow stress of the solid grains, (ii) rate effects of interstitial liquid flow, and (iii) inertial effects of grain rearrangement in a dense granular assembly. To explore the importance of the viscoplastic deformation of the solid phase to the rate sensitivity, the simulations for the 84%PK case were repeated with the strain rate sensitivity of the solid turned off (using a constant solid flow stress of $F_y - F_0 = 1.6 \times 10^{-9}$ N at all rates), as

shown in Fig. 11. With the strain-rate sensitive grains (left column of Fig. 11), the $1\mu m \cdot s^{-1}$ simulation shows high local contraction (vol. strain -0.25) ahead of the push-plate, and the compaction zone becomes less contractive with increasing displacement rate (vol. strain -0.18 in $30\mu m \cdot s^{-1}$ and -0.05 in $2150\mu m \cdot s^{-1}$) and a larger area undergoing dilation (red regions). When the strain-rate sensitivity is removed (middle column of Fig. 11), the magnitude of contraction in the compaction zone ahead of the push-plate is less sensitive to the displacement rate. These simulations show that, for strain rate sensitive grains, the lower flow stress at low shear rate gives more viscoplastic deformation of the grains. This has most influence just ahead of the push-plate where the stresses are highest; here more viscoplastic deformation of the solid phase expels more liquid similar to the compressive deformation of a liquid-saturated sponge and appears as high contraction in the volumetric strain fields. This can also be seen in Fig. 7.

To further understand the rate effects of interstitial liquid flow, three simulations without strain-rate sensitivity to the flow stress of solid were repeated without the interstitial liquid (i.e., with LBM turned off, skipping calculations from step 9 to step 17 in Fig. 2, resulting in no liquid drag force or moment on DEM grains). As shown in the right column of Fig. 11, the magnitude of contraction ahead of the push-plate is ~ -0.2 for all displacement rates when taking out the effects of interstitial liquid flow. The greater contraction in the compaction zone for the dry $30\mu m \cdot s^{-1}$ and $2150\mu m \cdot s^{-1}$ simulations in comparison to the coupled LBM-DEM simulations (the middle column of Fig. 11) is because the effect of the interstitial liquid, which suppresses further deformation by local liquid pressure increase, was removed. Besides, the simulations without liquid have a band of dilation (red) enclosing the compaction zone ahead of push-plate instead of multiple pockets of dilatant regions in coupled LBM-DEM simulations, especially at $2150\mu m \cdot s^{-1}$. Some contraction in the far-right side of FOV for $30\mu m \cdot s^{-1}$ and $2150\mu m \cdot s^{-1}$ LBM-DEM simulations, which is due to the

suction of liquid away to the dilating regions along the parting plane, becomes less contractive in the no liquid (no-LBM) simulations.

At the same time, it is clear in Fig. 11 that removing the strain rate sensitivity of the solid and the effects of interstitial liquid does not eliminate the strain rate dependence of the contraction/dilation behaviour. Especially, the volumetric strain field $\varepsilon_{xx} + \varepsilon_{yy}$ and total volumetric strain $\varepsilon_{vol}^{\text{DEM}}$ in 2150µm·s^{-1} simulations are still more positive (dilative) than 30µm·s^{-1} simulations. This phenomenon can be related to the "inertial effect" of granular assemblies investigated in 2D DEM simple shear tests [120] and annular shear experiments on spherical polystyrene beads [121] previously. Those studies proposed that grain-grain interactions in granular materials at high deformation rate are dominated by binary collisions rather than forming a well-defined force chain network as in low-rate granular deformation. Such rate-dependent rheology of granular materials can be quantified using a dimensionless "inertial number", $I_{\dot\gamma}$ [120]:

$$I_{\dot\gamma} = \dot\gamma \sqrt{\frac{m_{\text{grain}}}{P}} \qquad (20)$$

where $\dot\gamma$ is the shear rate, m_{grain} is the mass of individual grains, and P is the confining pressure in 2D. Granular deformation is in the "quasistatic critical state" regime if a system has $I_{\dot\gamma} \leq 10^{-3}$ which corresponds to low shear rate deformation where the confining pressure dominates over inertial effects. When $I_{\dot\gamma} \geq 10^{-1}$ deformation is in the "collisional flow" regime corresponding to high shear rate deformation where inertial effects are dominant. This regime has distinctively lower critical solid fraction for the transition from net contraction to net dilation, $f_{S.pk}^{c}$, than the quasistatic regime, and a linear decrease of 2D critical solid fraction against $I_{\dot\gamma}$ in the intermediate "dense flow regime" ($10^{-3} \leq I_{\dot\gamma} \leq 10^{-1}$) was found [120], which is named a "dynamic dilatancy" law:

$$f_{S.pk}^{c}(I_{\dot\gamma}) \approx f_{S.pk}^{c.max} - aI_{\dot\gamma} \qquad\qquad (21)$$

where $f_{S.pk}^{c.max} \approx 81\%$ and $a \approx 0.3$ for $\pm 20\%$ polydispersity, quasi-rigid circlular DEM grains with contact friction coefficient $\mu = 0.4$ [120]. For the simulations in this paper, the inertial number in Eq. (20) can be calculated with the assumption of $\dot\gamma \approx \frac{du_y/dt}{10\text{mm}}$; taking the effective mean stress acting on the solid, p', from the simulations as the pressure; and taking $m_{\text{grain}} \approx 0.25\rho\pi\bar{d}^2$. With this approach, the $1\mu\text{m·s}^{-1}$ and $30\mu\text{m·s}^{-1}$ simulations all have $I_{\dot\gamma} \leq 0.002$ and can be regarded as quasi-static. The $2150\mu\text{m·s}^{-1}$ simulations have $I_{\dot\gamma} \approx 10^{-1}$, which falls into the "dense flow" regime with intrinsically lower critical solid fraction for the transition from net contraction to net dilation, $f_{S.pk}^{c}$.

We note that this study has been conducted in the shear rate range $10^{-4} \leq \dot\gamma \leq 10^{-1}$ s^{-1} and deformation in semi-solid processing and pressurised casting processes can be significantly higher than this. While further work is required to confirm the mechanisms at higher shear rate, it is likely that higher shear rates will further suppress individual grain deformation, increase interstitial liquid pressure gradients, and encourage collisional flow.

3.5. The transition to shear cracking

All six shear cracking datasets (red experiments in Fig. 3j) involved either (i) the growth of a meniscus perpendicular to the X-ray beam from a pre-existing free surface or pore ("mechanism A" in Fig. 12a), and/or (ii) the growth of a meniscus parallel to the X-ray beam from the free surface ("mechanism B" in Fig. 12b). The underlying cause of both is the liquid pressure drop due to unfed shear-induced dilation. These two shear-cracking mechanisms can be seen in the two ROIs in the 57% - $2150\mu\text{m·s}^{-1}$ dataset shown in Fig. 12c, where the red ROI corresponds to "mechanism A" and the blue ROI to "mechanism B". As shown in Fig.

12c and d, the "mechanism A" crack initiates from a pre-existing pore, and grows into a liquid-filled fissure by the propagation of a liquid-air meniscus. In the $u_y = 12.9\bar{d}$ snapshot in Fig. 12d, the meniscus touches a liquid fissure and soon grows into it ($u_y = 15.3\bar{d}$). Note that the time from $u_y = 12.9\bar{d}$ to $u_y = 15.3\bar{d}$ is only 0.12s, which limits the process of liquid feeding from adjacent semi-solid regions.

The "mechanism B" crack shown in Fig. 12c and e starts from a liquid-filled fissure ($u_y = 6.0\bar{d}$ and $9.0\bar{d}$ snapshots). The liquid then gradually becomes brighter from $u_y = 12.0\bar{d}$, indicating a reduction of liquid thickness through the X-ray beam direction in response to the decreasing liquid pressure. Note that in both the shear-cracking examples in Fig. 12d and e the grains adjacent to the crack do not detach from each other or fall under gravity because the meniscus generates a grain-grain suction force to minimise the gas-liquid surface area. Thus, the material is now in a partially saturated or unsaturated state to use the soil mechanics terminology [122], which is different from the cohesionless and fully-saturated regions away from cracking regions.

To understand the cracking process in Fig. 12e, an X-ray intensity line scan spanning the fissure/crack was studied, as indicated in Fig. 12f. The corresponding transmitted X-ray intensity profiles along this line from prior to deformation ($u_y = 0\bar{d}$) to $u_y = 24\bar{d}$ are shown in Fig. 12g, where the middle of the opening liquid fissure is set to have relative $y = 0$ and the intensity profiles change from a cold to a hot colour with increasing displacement. The shape of the meniscus (similar to Fig. 12b) was found by calculating the thickness of the semi-solid sample, L_{alloy}^{n}, from the X-ray intensity derived using Eq. (2) and defining the nominal relative z-position as:

$$z(x_{\text{vert}}, y) = \pm \frac{L_{alloy}^{n}(x_{\text{vert}}, y)}{2} \qquad (22)$$

where x_{vert} is the x-position of the yellow vertical line in Fig. 12f. Fig. 12h shows the result from this approach: both a significant localised reduction in thickness, and a smaller reduction in thickness in the bulk semi-solid from $L_{alloy}^0 \approx 150\mu m$ to $L_{alloy}^n \approx 140\mu m$ are observed. The reduction of the radius of curvature, R, of the meniscus in the y-z plane offers insights into the drop of liquid pressure Δp using the Young-Laplace equation:

$$\Delta p \approx -\frac{2\gamma}{R} \tag{23}$$

where γ is the liquid-air interfacial energy $\approx 0.7 \text{ J/m}^2$ [123]. Fig. 12h shows that the radius of curvature at $u_y = 12.0\bar{d}$ is ≈ 400 μm corresponding to $\Delta p \approx -1.75$kPa, and the radius of curvature then reduces to ≈ 100 μm when $u_y = 24.0\bar{d}$ with a drop of Δp to -14.00kPa. The evaluated Young-Laplace pressure Δp of -14 kPa is comparable to a shear-cracking example measured in high solid fraction steel previously [32, 124], in which the change in liquid pressure of -10 kPa was estimated.

It was found that a reasonable criterion for shear cracking in the simulations is that the first meniscus is drawn-in when the liquid pressure drop reaches a critical value, set here as $\Delta p_c = -0.03$Pa for the 2D LBM (Fig. 10). The change of the liquid pressure $\Delta p(\mathbf{x}_i, t)$ in Fig. 10 shows that the 4x3 matrix of simulations reproduce the main phenomena from the experiments. For example, the location where the critical pressure drop is first reached is adjacent to or above the top-right corner of the push-plate, in good agreement with the first cracking location in the experiments (Fig. 12j). This region has more positive local volumetric strain ($\varepsilon_{xx} + \varepsilon_{yy}$, Fig. 8) and shear strain (ε_{xy}, Fig. 9) as well. Also, taking the critical pressure drop as the criterion for cracking, it can be seen that: (i) for the same initial solid fraction, a transition from no-cracking to cracking occurs as the shear rate increases; (ii) the critical shear rate for the cracking transition is lower for higher initial solid fraction; and

(iii) for the same displacement rate, a transition from no-cracking to cracking occurs as the initial solid fraction increases, each in agreement with the experiments. For the $30\mu m \cdot s^{-1}$ and $2150\mu m \cdot s^{-1}$ simulations, the transition from no-cracking to cracking occurs when the total (dilatational) volumetric strain $\varepsilon_{vol}^{DEM} > 5\%$. The $1\mu m \cdot s^{-1}$ simulations and experiment are less susceptible to cracking within $u_y < 10.0\bar{d}$ unless the solid fraction is very high (e.g., $g_S^0 = 93\%$ in ref. [35]). The concept of a threshold Δp_c used here is essentially similar to the critical "cavitation pressure" in the Rappaz-Drezet-Gremaud (RDG) hot-tearing criterion [125] although, here, the samples are under compressive deformation.

4. Conclusions

The transition of semi-solid deformation behaviour from suspension flow to granular deformation, and the onset of shear cracking have been investigated by radiographic imaging of the deformation of thin samples of equiaxed globular Al-Cu alloys at $38 - 85\%$ volumetric solid fraction under strain rates in the interval $10^{-4} - 10^{-1}$ s^{-1}. X-ray intensity processing was used to analyse a range of semi-solid deformation phenomena such as the percolation of the α-Al grains, contraction or dilation of the assembly in response to loading, and the drop of liquid pressure during the shear-cracking process. These phenomena were further explored using a 2D LBM-DEM model created using the initial microstructures quantified in the experiments. From the deformation microstructures observed under various solid fractions and strain rates, the following conclusions can be drawn:

- The percolation threshold of equiaxed globular grains in the experiments is ~38 vol%; similar packing phenomena were modelled in the coupled LBM-DEM approach using buoyant grains, which gave a 2D packing limit of ~77%.

- In addition to the role of initial solid fraction on contraction/dilation response that

has been linked to the critical state framework for soil behaviour previously, the contraction-to-dilation transition is shown here to be strain-rate dependent. Shear deformation experiments and simulations both show that a higher strain rate will lead to additional shear-induced dilation.

- Simulations show that the rate effects have at least three components: (i) the strain-rate sensitivity to the flow stress of the solid, (ii) rate effects of interstitial liquid flow, and (iii) inertial effects of grain rearrangement with higher rates increasing the possibility of binary grain-grain collisions similar dense gases under strong agitation.

- The location of the first cracking observed in the shear deformation experiments is adjacent to or above the top-right corner of the push-plate, which is in good correlation with the location where highly positive volumetric strain, shear strain, and more drop of liquid pressure occur in simulations.

- Both experiments and simulations show that the critical shear rate for the cracking transition is lower for higher initial solid fractions, and the cracking transition is highly strain rate dependent. This indicates the significant influence of time-dependent dissipation processes of the excess liquid pressure on the onset of shear cracking.

Acknowledgements

References

[1] A. Kaye, A. Street, Die Casting Metallurgy, Butterworth Scientific, London, 1982.

[2] W. Andresen, Die Cast Engineering: A Hydraulic, Thermal, and Mechanical Process, CRC Press, New York, 2004.

[3] M.S. Dargusch, G. Dour, N. Schauer, C.M. Dinnis, G. Savage, The influence of pressure during solidification of high pressure die cast aluminium telecommunications components, J. Mater. Process. Technol. 180(1-3) (2006) 37-43.

[4] G. Timelli, O. Lohne, L. Arnberg, H.I. Laukli, Effect of solution heat treatments on the microstructure and mechanical properties of a die-cast AlSi7MgMn alloy, Metall. Mater. Trans. A 39A(7) (2008) 1747-1758.

[5] R. Cook, P.G. Grocock, P.M. Thomas, D.V. Edmonds, J.D. Hunt, Development of the twin-roll casting process, J. Mater. Process. Technol. 55(2) (1995) 76-84.

[6] C. Gras, M. Meredith, J.D. Hunt, Microdefects formation during the twin-roll casting of Al-Mg-Mn aluminium alloys, J. Mater. Process. Technol. 167(1) (2005) 62-72.

[7] Z. Bian, I. Bayandorian, H.W. Zhang, G. Scamans, Z. Fan, Extremely fine and uniform microstructure of magnesium AZ91D alloy sheets produced by melt conditioned twin roll casting, Mater. Sci. Technol. 25(5) (2009) 599-606.

[8] T. Koshikawa, M. Bellet, C.A. Gandin, H. Yamamura, M. Bobadilla, Experimental study and two-phase numerical modeling of macrosegregation induced by solid deformation during punch pressing of solidifying steel ingots, Acta Mater. 124 (2017) 513-527.

[9] R. Thome, K. Harste, Principles of billet soft-reduction and consequences for continuous casting, ISIJ Int. 46(12) (2006) 1839-1844.

[10] M.C. Flemings, Solidification Processing, McGraw-Hill, New York, 1974.

[11] S. Otarawanna, H.I. Laukli, C.M. Gourlay, A.K. Dahle, Feeding mechanisms in high-pressure die castings, Metall. Mater. Trans. A 41A(7) (2010) 1836-1846.

[12] C.P. Chen, C.Y.A. Tsao, Semi-solid deformation of non-dendritic structures. 1. Phenomenological behavior, Acta Mater. 45(5) (1997) 1955-1968.

[13] M.S. Kim, S.H. Kim, H.W. Kim, Deformation-induced center segregation in twin-roll cast high-Mg Al–Mg strips, Scr. Mater. 152 (2018) 69-73.

[14] Y. Zhang, J.B. Patel, Y. Wang, Z. Fan, Variation improvement of mechanical properties of Mg-9Al-1Zn alloy with melt conditioned high pressure die casting, Mater. Charact. 144 (2018) 498-504.

[15] E. Lordan, J. Lazaro-Nebreda, Y.J. Zhang, Z.Y. Fan, Effective degassing for reduced variability in high-pressure die casting performance, JOM 71(2) (2019) 824-830.

[16] S.M. Lee, H.H. Kim, C.G. Kang, The effect of applied forging pressure on primary structure deformation in rheology forging process with solid fraction controlled A356 and AA2024 alloys, J. Eng. Mater.-T. Asme 132(2) (2010) 021015-021015-7.

[17] S. Otarawanna, C.M. Gourlay, H.I. Laukli, A.K. Dahle, Microstructure formation in AlSi4MgMn and AlMg5Si2Mn high-pressure die castings, Metall. Mater. Trans. A 40A(7) (2009) 1645-1659.

[18] C.M. Gourlay, A.K. Dahle, Dilatant shear bands in solidifying metals, Nature 445(7123) (2007) 70-73.

[19] B. Meylan, S. Terzi, C.M. Gourlay, A.K. Dahle, Dilatancy and rheology at 0-60% solid during equiaxed solidification, Acta Mater. 59(8) (2011) 3091-3101.

[20] C.M. Gourlay, B. Meylan, A.K. Dahle, Shear mechanisms at 0-50% solid during equiaxed dendritic solidification of an AZ91 magnesium alloy, Acta Mater. 56(14) (2008) 3403-3413.

[21] E. Tzimas, A. Zavaliangos, Mechanical behavior of alloys with equiaxed microstructure in the semisolid state at high solid content, Acta Mater. 47(2) (1999) 517-528.

[22] T. Sumitomo, D.H. StJohn, T. Steinberg, The shear behaviour of partially solidified Al-Si-Cu alloys, Mater. Sci. Eng. A 289(1-2) (2000) 18-29.

[23] J.K. Mitchell, K. Soga, Fundamentals of Soil Behavior, 3rd ed., Wiley, New York, 1993.

[24] W. Powrie, Soil Mechanics: Concepts and Applications, 2nd ed., Taylor & Francis, New York, 2004.

[25] A. Schofield, P. Wroth, Critical State Soil Mechanics, McGraw-Hill, New York, 1968.

[26] O. Reynolds, LVII. On the dilatancy of media composed of rigid particles in contact. With experimental illustrations, Philos. Mag. Series 5 20(127) (1885) 469-481.

[27] C.M. Gourlay, A.K. Dahle, T. Nagira, N. Nakatsuka, K. Nogita, K. Uesugi, H. Yasuda, Granular deformation mechanisms in semi-solid alloys, Acta Mater. 59(12) (2011) 4933-4943.

[28] C.M. Gourlay, C. O'Sullivan, J. Fonseca, L. Yuan, K.M. Kareh, T. Nagira, H. Yasuda, Synchrotron radiography studies of shear-induced dilation in semisolid Al alloys and steels, JOM 66(8) (2014) 1415-1424.

[29] T. Nagira, C.M. Gourlay, A. Sugiyama, M. Uesugi, Y. Kanzawa, M. Yoshiya, K. Uesugi, K. Umetani, H. Yasuda, Direct observation of deformation in semi-solid carbon steel, Scr. Mater. 64(12) (2011) 1129-1132.

[30] T. Nagira, H. Yokota, S. Morita, H. Yasuda, M. Yoshiya, C.M. Gourlay, A. Sugiyama, K. Uesugi, K. Umetani, Characterization of shear deformation based on in-situ observation of deformation in semi-solid Al-Cu alloys and water-particle mixture, ISIJ Int. 53(7) (2013) 1195-1201.

[31] J. Fonseca, C. O'Sullivan, T. Nagira, H. Yasuda, C.M. Gourlay, In situ study of granular micromechanics in semi-solid carbon steels, Acta Mater. 61(11) (2013) 4169-4179.

[32] T. Nagira, S. Morita, H. Yokota, H. Yasuda, C.M. Gourlay, M. Yoshiya, A. Sugiyama, K. Uesugi, A. Takeuchi, Y. Suzuki, In situ observation of deformation in semi-solid Fe-C alloys at high shear rate, Metall. Mater. Trans. A 45A(12) (2014) 5613-5623.

[33] S. Zabler, A. Rack, A. Rueda, L. Helfen, F. Garcia-Moreno, J. Banhart, Direct observation of particle flow in semi-solid alloys by synchrotron X-ray micro-radioscopy,

Physica Status Solidi A 207(3) (2010) 718-723.

[34] S. Zabler, A. Ershov, A. Rack, F. Garcia-Moreno, T. Baumbach, J. Banhart, Particle and liquid motion in semi-solid aluminium alloys: a quantitative in situ microradioscopy study, Acta Mater. 61(4) (2013) 1244-1253.

[35] K.M. Kareh, P.D. Lee, R.C. Atwood, T. Connolley, C.M. Gourlay, Revealing the micromechanisms behind semi-solid metal deformation with time-resolved X-ray tomography, Nat. Commun. 5 (2014) 1-7.

[36] B. Cai, P.D. Lee, S. Karagadde, T.J. Marrow, T. Connolley, Time-resolved synchrotron tomographic quantification of deformation during indentation of an equiaxed semi-solid granular alloy, Acta Mater. 105 (2016) 338-346.

[37] S. Terzi, L. Salvo, M. Suery, N. Limodin, J. Adrien, E. Maire, Y. Pannier, M. Bornert, D. Bernard, M. Felberbaum, M. Rappaz, E. Boller, In situ X-ray tomography observation of inhomogeneous deformation in semi-solid aluminium alloys, Scr. Mater. 61(5) (2009) 449-452.

[38] A. Zavaliangos, Modeling of the mechanical behavior of semisolid metallic alloys at high volume fractions of solid, Int. J. Mech. Sci. 40(10) (1998) 1029-1041.

[39] J.J. Wang, A.B. Phillion, G.M. Lu, Development of a visco-plastic constitutive modeling for thixoforming of AA6061 in semi-solid state, J. Alloy Compd. 609 (2014) 290-295.

[40] X. Hu, Q. Zhu, H. Atkinson, H. Lu, F. Zhang, H. Dong, Y. Kang, A time-dependent power law viscosity model and its application in modelling semi-solid die casting of 319s alloy, Acta Mater. 124 (2017) 410-420.

[41] V. Favier, P. Cezard, R. Bigot, Transient and non-isothermal semi-solid behaviour: 3D micromechanical modelling, Mater. Sci. Eng. A 517(1-2) (2009) 8-16.

[42] V. Favier, H.V. Atkinson, Micromechanical modelling of the elastic-viscoplastic response of metallic alloys under rapid compression in the semi-solid state, Acta Mater. 59(3) (2011) 1271-1280.

[43] O. Ludwig, J.M. Drezet, C.L. Martin, M. Suery, Rheological behavior of Al-Cu alloys during solidification: constitutive modeling, experimental identification, and numerical study, Metall. Mater. Trans. A 36A(6) (2005) 1525-1535.

[44] O. Ludwig, J.M. Drezet, P. Meneses, C.L. Martin, M. Suery, Rheological behavior of a commercial AA5182 aluminum alloy during solidification, Mater. Sci. Eng. A 413 (2005) 174-179.

[45] G.M. Laschet, H. Behnken, Thermo-elasto-viscoplastic constitutive laws for metallic alloys during their solidification, IOP Conf. Ser.: Mater. Sci. Eng. 529 (2019) 012083.

[46] S. Benke, S. Dziallach, G. Laschet, U. Prahl, W. Bleck, Modeling of the uniaxial tensile and compression behavior of semi-solid A356 alloys, Comput. Mater. 45(3) (2009) 633-637.

[47] L.C. Nicolli, A. Mo, M. M'Hamdi, Modeling of macrosegregation caused by volumetric deformation in a coherent mushy zone, Metall. Mater. Trans. A 36A(2) (2005) 433-442.

[48] C.M.G. Rodrigues, A. Ludwig, M. Wu, A. Kharicha, A. Vakhrushev, A comprehensive analysis of macrosegregation formation during twin-roll casting, Metall. Mater. Trans. B 50(3) (2019) 1334-1350.

[49] L. Heyvaert, M. Bedel, M. Zaloznik, H. Combeau, Modeling of the coupling of microstructure and macrosegregation in a direct chill cast Al-Cu billet, Metall. Mater. Trans. A 48A(10) (2017) 4713-4734.

[50] T. Kajitani, J.M. Drezet, M. Rappaz, Numerical simulation of deformation-induced segregation in continuous casting of steel, Metall. Mater. Trans. A 32(6) (2001) 1479-1491.

[51] C.S. Li, B.G. Thomas, Thermomechanical finite-element model of shell behavior in continuous casting of steel, Metall. Mater. Trans. B 35(6) (2004) 1151-1172.

[52] J. Domitner, M.H. Wu, A. Kharicha, A. Ludwig, B. Kaufmann, J. Reiter, T. Schaden, Modeling the effects of strand surface bulging and mechanical soft reduction on the

macrosegregation formation in steel continuous casting, Metall. Mater. Trans. A 45A(3) (2014) 1415-1434.

[53] S. Vernede, J.A. Dantzig, M. Rappaz, A mesoscale granular model for the mechanical behavior of alloys during solidification, Acta Mater. 57(5) (2009) 1554-1569.

[54] M. Sistaninia, A.B. Phillion, J.M. Drezet, M. Rappaz, A 3-D coupled hydromechanical granular model for simulating the constitutive behavior of metallic alloys during solidification, Acta Mater. 60(19) (2012) 6793-6803.

[55] M. Sistaninia, A.B. Phillion, J.M. Drezet, M. Rappaz, Simulation of semi-solid material mechanical behavior using a combined discrete/finite element method, Metall. Mater. Trans. A 42A(1) (2011) 239-248.

[56] M. Sistaninia, S. Terzi, A.B. Phillion, J.M. Drezet, M. Rappaz, 3-D granular modeling and in situ X-ray tomographic imaging: a comparative study of hot tearing formation and semi-solid deformation in Al-Cu alloys, Acta Mater. 61(10) (2013) 3831-3841.

[57] M.H. Sheikh-Ansari, M. Aghaie-Khafri, Shear localization in semi-solid deformation: a bifurcation theory approach, Mech. Res. Commun. 89 (2018) 1-5.

[58] M.S. Ansari, M. Aghaie-Khafri, Predicting flow localization in semi-solid deformation, Int. J. Mater. Form. 11(2) (2018) 165-173.

[59] M.H. Sheikh-Ansari, M. Aghaie-Khafri, Constitutive modeling of semisolid deformation for the assessment of dilatant shear bands, Appl. Math. Model. 70 (2019) 128-138.

[60] M.H. Sheikh-Ansari, M. Aghaie-Khafri, An extension of Rice localization criterion to predict the onset of shear localization in semi-solid materials, Int. J. Mater. Form. (2018).

[61] L. Yuan, C. O'Sullivan, C.M. Gourlay, Exploring dendrite coherency with the discrete element method, Acta Mater. 60(3) (2012) 1334-1345.

[62] T.C. Su, C. O'Sullivan, T. Nagira, H. Yasuda, C.M. Gourlay, Semi-solid deformation of Al-Cu alloys: a quantitative comparison between real-time imaging and coupled LBM-DEM simulations, Acta Mater. 163 (2019) 208-225.

[63] B.K. Cook, D.R. Noble, J.R. Williams, A direct simulation method for particle-fluid systems, Eng Computation 21(2-4) (2004) 151-168.

[64] D. Noble, J. Torczynski, A lattice-Boltzmann method for partially saturated computational cells, Int. J. Mod. Phys. C 9(08) (1998) 1189-1201.

[65] Y.H. Han, P.A. Cundall, Resolution sensitivity of momentum-exchange and immersed boundary methods for solid-fluid interaction in the lattice Boltzmann method, Int. J. Numer. Meth. Fl. 67(3) (2011) 314-327.

[66] Y.H. Han, P.A. Cundall, LBM-DEM modeling of fluid-solid interaction in porous media, Int. J. Numer. Anal. Met 37(10) (2013) 1391-1407.

[67] D.H. Johnson, F. Vahedifard, B. Jelinek, J.F. Peters, Micromechanics of undrained response of dilative granular media using a coupled DEM-LBM model: a case of biaxial test, Comput. Geotech. 89 (2017) 103-112.

[68] K. Soga, K. Kumar, G. Biscontin, M. Kuo, Geomechanics from Micro to Macro, CRC Press, London, 2014.

[69] A.J.C. Ladd, Numerical simulations of particulate suspensions via a discretized Boltzmann-equation. 1. Theoretical foundation, J. Fluid Mech. 271 (1994) 285-309.

[70] H. Yasuda, I. Ohnaka, K. Kawasaki, A. Suglyama, T. Ohmichi, J. Iwane, K. Umetani, Direct observation of stray crystal formation in unidirectional solidification of Sn-Bi alloy by X-ray imaging, J. Cryst. Growth 262(1-4) (2004) 645-652.

[71] H. Yasuda, Y. Yamamoto, N. Nakatsuka, M. Yoshiya, T. Nagira, A. Sugiyama, I. Ohnaka, K. Uesugi, K. Umetani, In situ observation of solidification phenomena in Al-Cu and Fe-Si-Al alloys, Int. J. Cast. Metals Res. 22(1-4) (2009) 15-21.

[72] H. Yasuda, T. Nagira, M. Yoshiya, N. Nakatsuka, A. Sugiyama, K. Uesugi, K. Umetani, Development of X-ray imaging for observing solidification of carbon steels, ISIJ Int. 51(3)

(2011) 402-408.

[73] C.M. Gourlay, K. Nogita, A.K. Dahle, Y. Yamamoto, K. Uesugi, T. Nagira, M. Yoshiya, H. Yasuda, In situ investigation of unidirectional solidification in Sn-0.7Cu and Sn-0.7Cu-0.06Ni, Acta Mater. 59(10) (2011) 4043-4054.

[74] K. Umetani, K. Uesugi, M. Kobatake, A. Yamamoto, T. Yamashita, S. Imai, Synchrotron radiation microimaging in rabbit models of cancer for preclinical testing, Nucl. Instrum. Methods Phys. Res. A 609(1) (2009) 38-49.

[75] D. Swinehart, The Beer-Lambert law, J. Chem. Educ. 39(7) (1962) 333.

[76] P.A. Cundall, A computer model for simulating progressive large scale movements in blocky rock systems, Proceedings of the International Symposium on Rock Fracture, ISRM, Nancy (F), 1971, pp. 2-8.

[77] C. O'Sullivan, Particulate Discrete Element Modelling: A Geomechanics Perspective, Spon, London, 2011.

[78] S. Chen, G.D. Doolen, Lattice Boltzmann method for fluid flows, Annu. Rev. Fluid. Mech. 30 (1998) 329-364.

[79] S.L. Han, P. Zhu, Z.Q. Lin, Two-dimensional interpolation-supplemented and Taylor-series expansion-based lattice Boltzmann method and its application, Commun. Nonlinear Sci. 12(7) (2007) 1162-1171.

[80] X.Y. He, L.S. Luo, Theory of the lattice Boltzmann method: from the Boltzmann equation to the lattice Boltzmann equation, Phys. Rev. E 56(6) (1997) 6811-6817.

[81] X.Y. He, L.S. Luo, A priori derivation of the lattice Boltzmann equation, Phys. Rev. E 55(6) (1997) R6333-R6336.

[82] R. Mei, W. Shyy, D. Yu, L.S. Luo, Lattice Boltzmann method for 3-D flows with curved boundary, J. Comput. Phys. 161(2) (2000) 680-699.

[83] H. Zhou, G.Y. Mo, F. Wu, J.P. Zhao, M. Rui, K.F. Cen, GPU implementation of lattice Boltzmann method for flows with curved boundaries, Comput. Method. Appl. M. 225 (2012) 65-73.

[84] L. Verlet, Computer" experiments" on classical fluids. I. Thermodynamical properties of Lennard-Jones molecules, Phys. Rev. 159(1) (1967) 98.

[85] A. Cottrell, R. Stokes, Effects of temperature on the plastic properties of aluminium crystals, Proceedings of the Royal Society of London A: Mathematical, Physical and Engineering Sciences, The Royal Society, 1955, pp. 17-34.

[86] M. Braccini, C.L. Martin, A. Tourabi, Y. Brechet, M. Suery, Low shear rate behavior at high solid fractions of partially solidified Al-8 wt.% Cu alloys, Mater. Sci. Eng. A 337(1-2) (2002) 1-11.

[87] S. Succi, The Lattice Boltzmann Equation for Fluid Dynamics and Beyond, Clarendon, Oxford, 2001.

[88] Q.S. Zou, X.Y. He, On pressure and velocity boundary conditions for the lattice Boltzmann BGK model, Phys. Fluids 9(6) (1997) 1591-1598.

[89] B.K. Cook, A Numerical Framework for the Direct Simulation of Solid-Fluid Systems, PhD thesis, Massachusetts Institute of Technology, US, 2001.

[90] O.E. Strack, B.K. Cook, Three-dimensional immersed boundary conditions for moving, solids in the lattice-Boltzmann method, Int. J. Numer. Meth. Fl. 55(2) (2007) 103-125.

[91] D.R.J. Owen, C.R. Leonardi, Y.T. Feng, An efficient framework for fluid-structure interaction using the lattice Boltzmann method and immersed moving boundaries, Int. J. Numer. Meth. Eng. 87(1-5) (2011) 66-95.

[92] L.M. Wang, G.F. Zhou, X.W. Wang, Q.G. Xiong, W. Ge, Direct numerical simulation of particle-fluid systems by combining time-driven hard-sphere model and lattice Boltzmann method, Particuology 8(4) (2010) 379-382.

[93] P.L. Bhatnagar, E.P. Gross, M. Krook, A model for collision processes in gases. I. Small

amplitude processes in charged and neutral one-component systems, Phys. Rev. 94(3) (1954) 511.

[94] X.Y. He, Q.S. Zou, L.S. Luo, M. Dembo, Analytic solutions of simple flows and analysis of nonslip boundary conditions for the lattice Boltzmann BGK model, J. Stat. Phys. 87(1-2) (1997) 115-136.

[95] U. Frisch, B. Hasslacher, Y. Pomeau, Lattice-gas automata for the Navier-Stokes equation, Phys. Rev. Lett. 56(14) (1986) 1505-1508.

[96] H.D. Chen, S.Y. Chen, W.H. Matthaeus, Recovery of the Navier-Stokes equations using a lattice-gas Boltzmann method, Phys. Rev. A 45(8) (1992) R5339-R5342.

[97] K.K. Soundararajan, Multi-Scale Multiphase Modelling of Granular Flows, PhD Thesis, University of Cambridge, UK, 2015.

[98] Y. Han, P. Cundall, Verification of two-dimensional LBM-DEM coupling approach and its application in modeling episodic sand production in borehole, Petroleum 3(2) (2017) 179-189.

[99] A.J.C. Ladd, R. Verberg, Lattice-Boltzmann simulations of particle-fluid suspensions, J. Stat. Phys. 104(5-6) (2001) 1191-1251.

[100] M. Oda, H. Kazama, Microstructure of shear bands and its relation to the mechanisms of dilatancy and failure of dense granular soils, Geotechnique 48(4) (1998) 465-481.

[101] Y.H. Wang, S.C. Leung, A particulate-scale investigation of cemented sand behavior, Can. Geotech. J. 45(1) (2008) 29-44.

[102] S. Ganesan, D.R. Poirier, Densities of aluminum-rich aluminum-copper alloys during solidification, Metall. Trans. A 18(4) (1987) 721-723.

[103] S. Ganesan, R. Speiser, D.R. Poirier, Viscosities of aluminum-rich Al−Cu liquid alloys, Metall. Trans. B 18(2) (1987) 421-424.

[104] M.J. Turner, Stiffness and deflection analysis of complex structures, J. Aeronaut. Sci. 23(9) (1956) 805-823.

[105] C. O'Sullivan, J.D. Bray, S.F. Li, A new approach for calculating strain for particulate media, Int. J. Numer. Anal. Met 27(10) (2003) 859-877.

[106] F. Dedecker, M. Chaze, P. Dubujet, B. Cambou, Specific features of strain in granular materials, Mech. Cohes.-Frict. Mat. 5(3) (2000) 173-193.

[107] N.L.M. Veldman, A.K. Dahle, D.H. St John, L. Arnberg, Dendrite coherency of Al-Si-Cu alloys, Metall. Mater. Trans. A 32(1) (2001) 147-155.

[108] L. Arnberg, G. Chai, L. Backerud, Determination of dendritic coherency in solidifying melts by theological measurements, Mater. Sci. Eng. A 173(1-2) (1993) 101-103.

[109] S.M. Nabulsi, The Behaviour of Partially Solidified Aluminium-Silicon Alloys in a Direct Shear Cell, PhD Thesis, The University of Queensland, Australia, 1997.

[110] C.M. Gourlay, Rheology of Solidifying Alloys Containing 0-50% Solid and the Formation of Dilatant Shear Bands, PhD Thesis, The University of Queensland, Australia, 2006.

[111] H. Wang, D.H. StJohn, C.J. Davidson, M.J. Couper, Characterization and shear behaviour of semisolid Al-7Si-0.35Mg alloy microstructures, Alum. Trans. 2(1) (2000) 57-66.

[112] L.E. Silbert, Jamming of frictional spheres and random loose packing, Soft Matter 6(13) (2010) 2918-2924.

[113] E.L. Hinrichsen, J. Feder, T. Jøssang, Random packing of disks in two dimensions, Phys. Rev. A 41(8) (1990) 4199-4209.

[114] G.T. Nolan, P.E. Kavanagh, Computer simulation of random packings of spheres with log-normal distributions, Powder Technol. 76(3) (1993) 309-316.

[115] G.W. Delaney, J.E. Hilton, P.W. Cleary, Defining random loose packing for nonspherical grains, Phys. Rev. E 83(5) (2011).

[116] G.Y. Onoda, E.G. Liniger, Random loose packings of uniform spheres and the dilatancy

onset, Phys. Rev. Lett. 64(22) (1990) 2727-2730.

[117] P.A. Joly, R. Mehrabian, Rheology of a partially solid alloy, J. Mater. Sci. 11(8) (1976) 1393-1418.

[118] D.B. Spencer, R. Mehrabian, M.C. Flemings, Rheological behavior of Sn-15 pct Pb in the crystallization range, Metall. Trans. 3(7) (1972) 1925-1932.

[119] M.C. Flemings, Behavior of metal-alloys in the semisolid state, Metall. Trans. A 22(5) (1991) 957-981.

[120] F. da Cruz, S. Emam, M. Prochnow, J.N. Roux, F. Chevoir, Rheophysics of dense granular materials: discrete simulation of plane shear flows, Phys. Rev. E 72(2) (2005).

[121] A. Fall, G. Ovarlez, D. Hautemayou, C. Meziere, J.N. Roux, F. Chevoir, Dry granular flows: rheological measurements of the mu(I)-rheology, J. Rheol. 59(4) (2015) 1065-1080.

[122] D.G. Fredlund, H. Rahardjo, Soil mechanics for unsaturated soils, John Wiley & Sons, New York, 1993.

[123] M. Syvertsen, Oxide skin strength on molten aluminum, Metall. Mater. Trans. B 37(3) (2006) 495-504.

[124] K.M. Kareh, C. O'Sullivan, T. Nagira, H. Yasuda, C.M. Gourlay, Dilatancy in semi-solid steels at high solid fraction, Acta Mater. 125 (2017) 187-195.

[125] M. Rappaz, J.M. Drezet, M. Gremaud, A new hot-tearing criterion, Metall. Mater. Trans. A 30(2) (1999) 449-455.
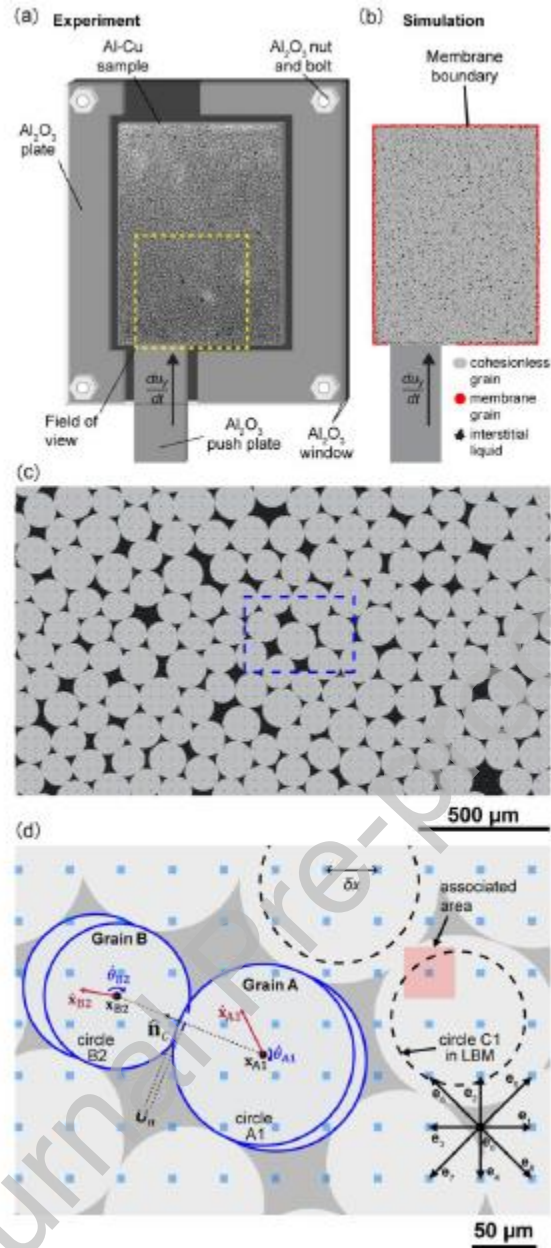
Fig. 1. (a) Schematic of the shear deformation cell sandwiched between two Al_2O_3 windows. Sample is 7.5 mm × 10.0 mm × ~0.2 mm. The dashed yellow square indicates the X-ray imaging field of view (FOV). (b) Simulated 2D grain assembly (light grey) saturated with liquid (dark grey), constrained by a push-plate and membrane (red). (c) Close-up view of the simulation sample. Both solid and liquid phases are overlain by LBM nodes (square blue dots). (d) Magnified view from the dashed blue rectangle in (c) showing contacting sub-grain circles A1 and B2 with centroids x_{A1}.and x_{B2}. The nine discretised velocities in LBM, e_α ($\alpha = 0 \sim 8$), are shown. $r_{hd} = 0.8$ here was used to reduce the radius of solid obstacles only in the LBM calculations. An associated area of an LBM node is drawn with corresponding local solid fraction $f_{S.xi} = 0.74$.
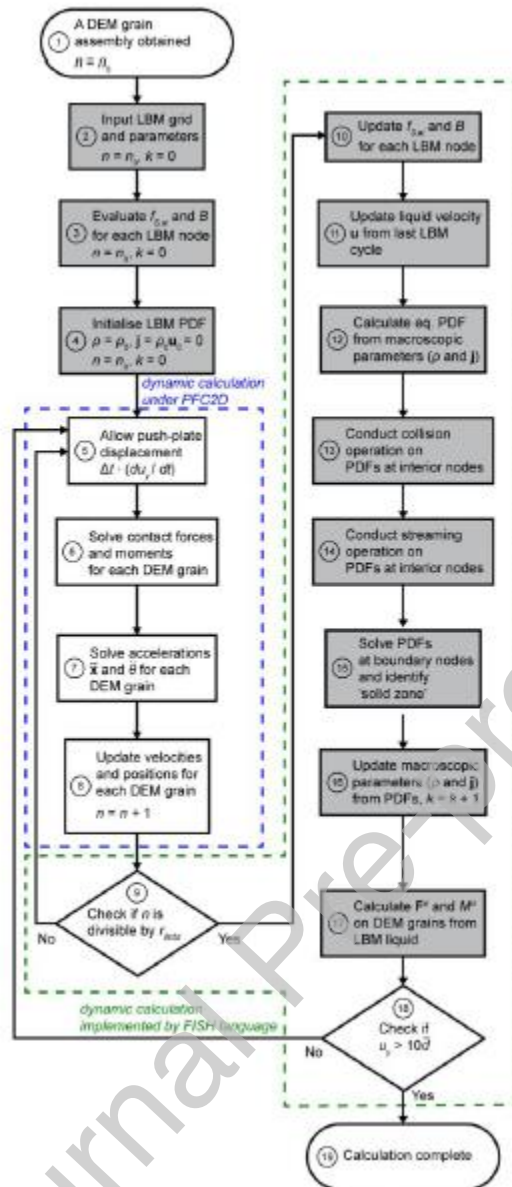
Fig. 2. Flow chart of the LBM-DEM coupling system. Blocks with white background indicate for DEM calculations to determine grain motion, and blocks filled by grey indicate the LBM calculations to determine the fluid flow and pressure.
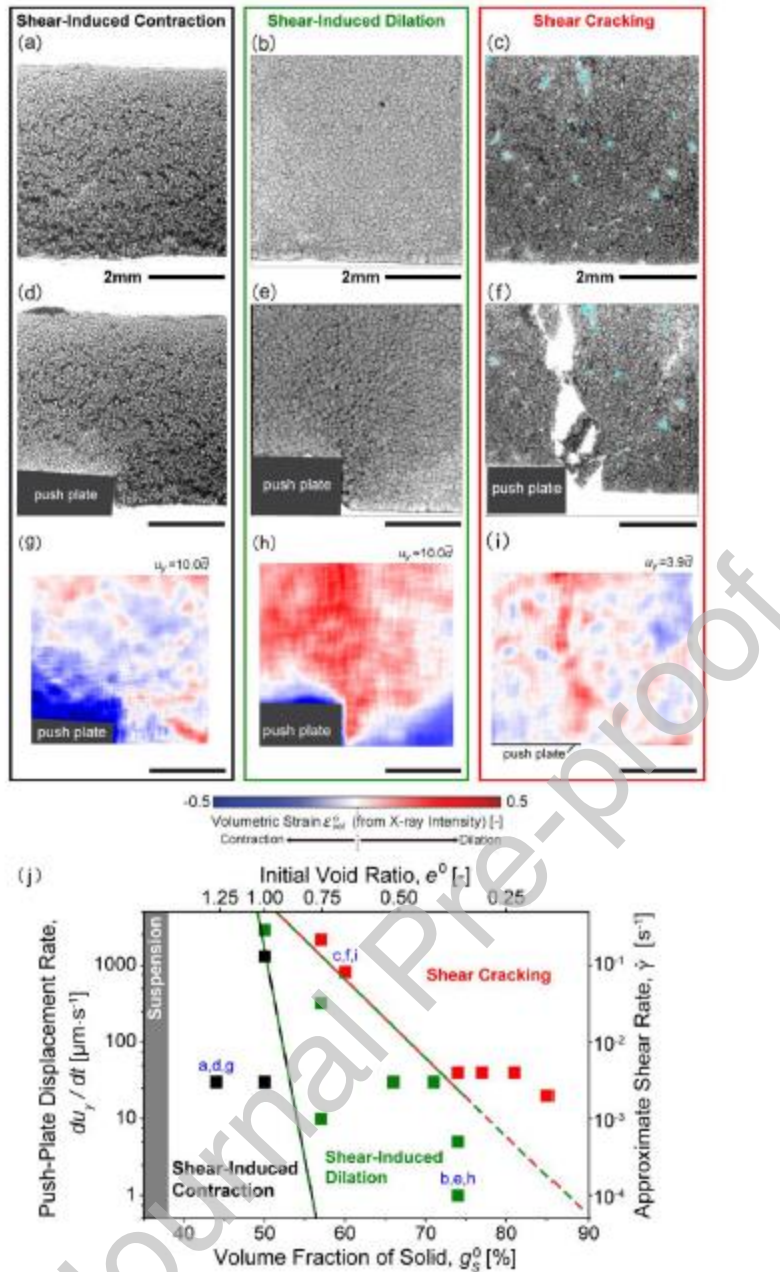
Fig. 3. (a-i) Examples of semi-solid deformation behaviours. Radiographs (a-c) are before shear, (d-f) are snapshots after a $10\bar{d}$ increment of push-plate displacement ($u_y = 10\bar{d}$), and (g-i) volumetric strain field, ε_{vol}^n, measured by X-ray intensity processing. (a,d,g) correspond to shear-induced contraction (44% - 30μm·s^{-1}); (b,e,h) to shear-induced dilation (74% - 1μm·s^{-1}), and (c,f,i) to shear cracking (60% - 820μm·s^{-1}). Pre-existing pores are indicated with cyan. Note that (d-h) are at $u_y = 10\bar{d}$, whereas (i) is at $u_y = 3.9\bar{d}$, i.e. just before cracking initiated. (j) A semi-logarithmic plot showing the influence of initial volume fraction of solid g_S^0 and rate of push plate displacement du_y/dt on deformation behaviour where "suspension" is indicated as grey, "shear-induced contraction" as black, "shear-induced dilation" as green, and "shear cracking" as red.
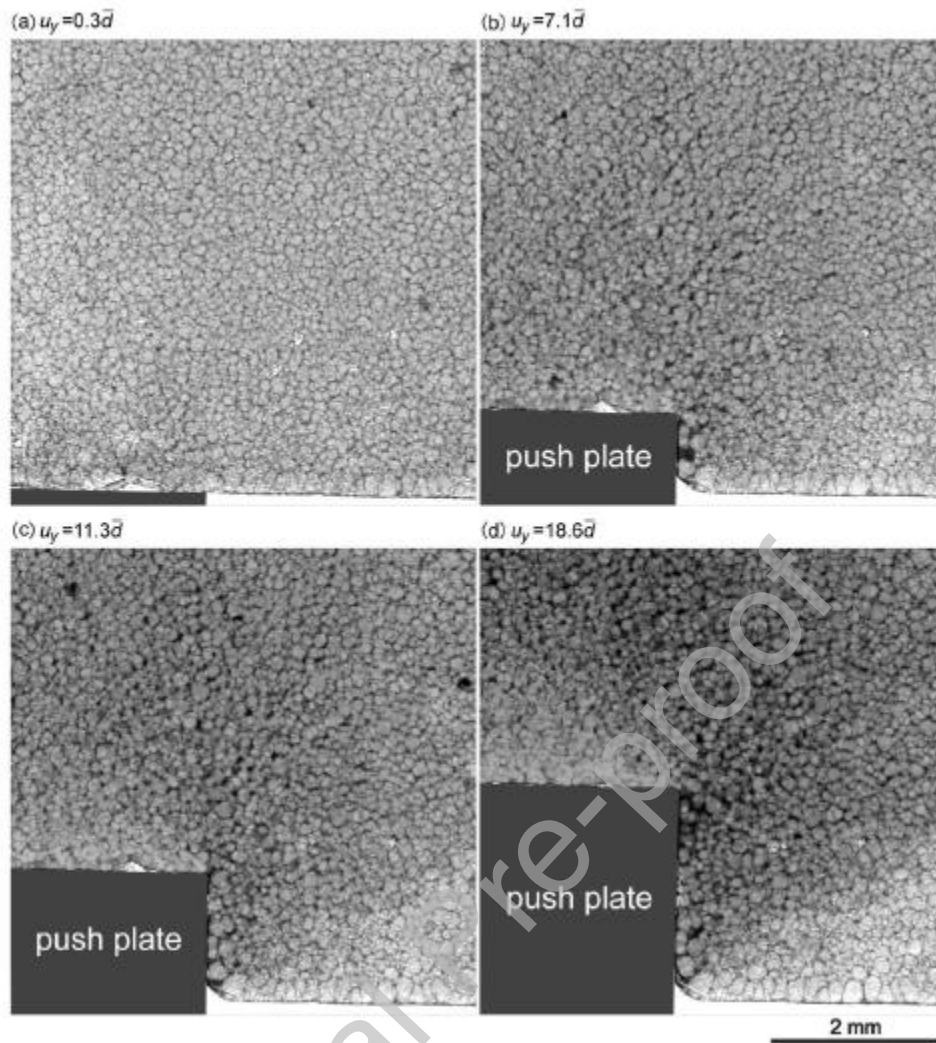
Fig. 4. Synchrotron radiography of shear-induced dilation during deformation at 74% - 1µm·s^{-1}. Liquid is dark, grains are bright.
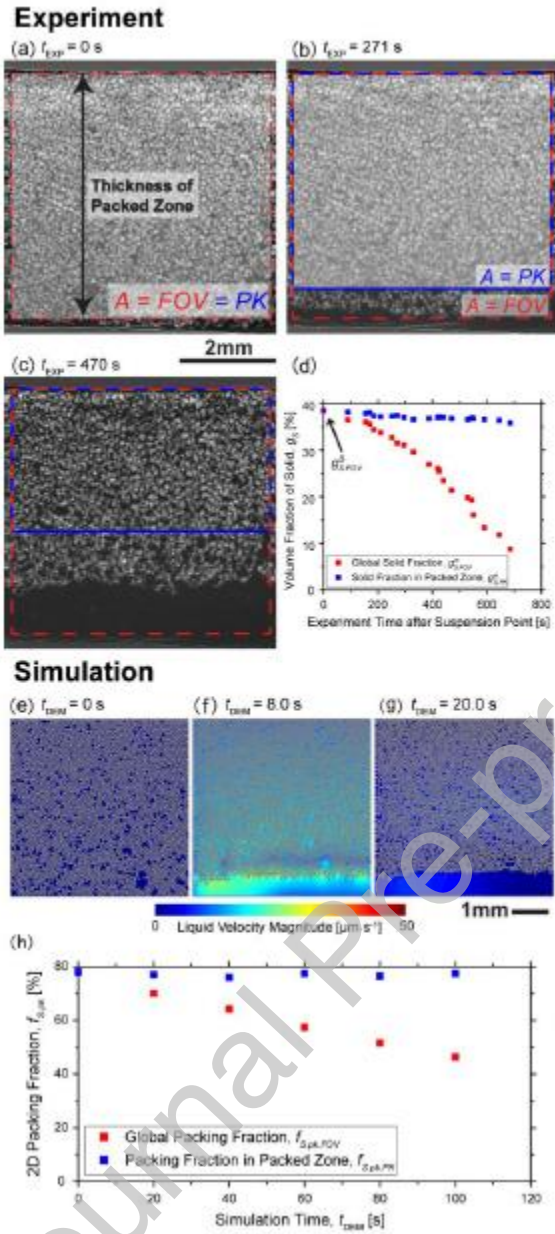
Fig. 5. (a-c) Radiographs showing the melting and floating of grains during in-situ heating experiment "38% - 0µm·s^{-1}": (a) a radiograph taken at the onset of grain floating ($t_{\mathrm{EXP}} = 0$ s). A dashed red ROI marking the region for measuring $g_{S.FOV}^0$. (b) During the heating experiment ($t_{\mathrm{EXP}} = 271$ s), the blue ROI indicates the approximate position of the packed zone (defined as a zone including grains having displacement < 2 µm within 10 seconds), and (c) a later stage of heating when $t_{\mathrm{EXP}} = 470$ s. The measuring area $A = FOV$ was fixed, while $A = PK$ is adjusted to follow the packed zone position. (d) Measurements of $g_{S.FOV}^n$ and $g_{S.PK}^n$ against experiment time, t_{EXP}. (e-g) LBM-DEM simulation of floating movement (Float - 0µm·s^{-1}): (e) the initial assembly before the buoyancy field affected the DEM grains, (f) a snapshot of the floating simulation with liquid velocity field overlapped ($t_{\mathrm{DEM}} = 8.0$ s), and (g) a packed assembly regenerated by floating grains. Only the left side of the simulated sample is shown in (e-g). (h) Measurement of $f_{S.pk}^n$ against simulation time, t_{DEM}.
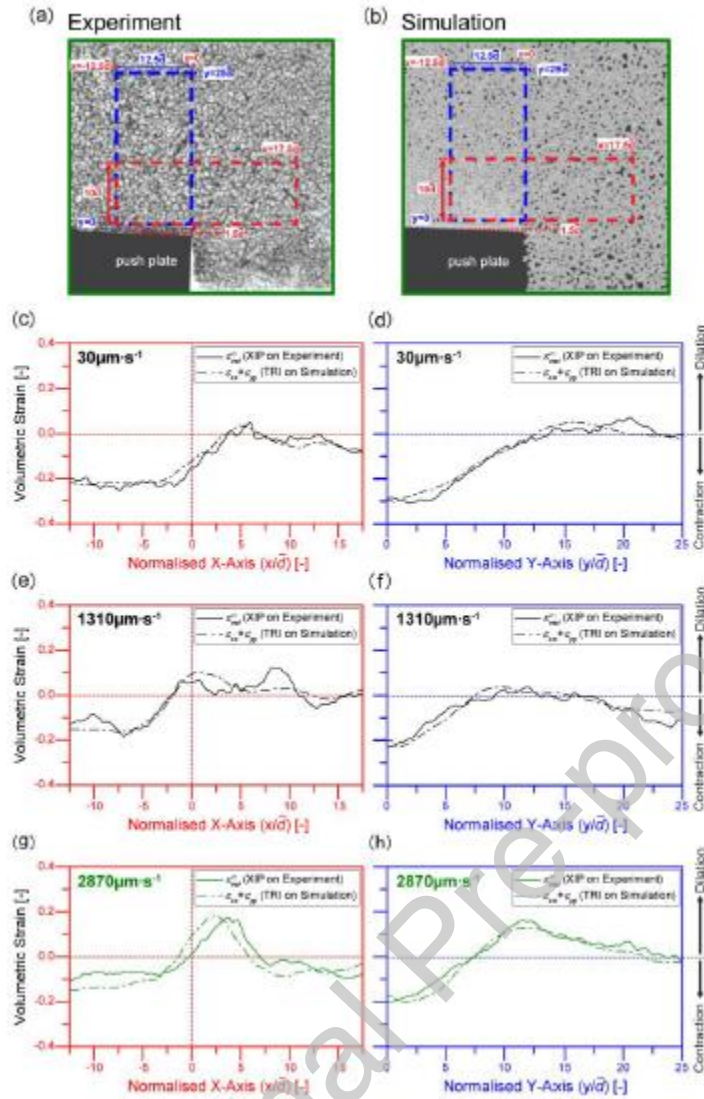
Fig. 6. Direct comparison of volumetric strain profiles from $g_S^0 = 50\%$ datasets and simulations I-III after $10\bar{d}$ increment of push-plate displacement, at three displacement rates. (a-b) The definition of two regions of interest (ROIs), red and blue, used to study volumetric strain. In (a) the 50% - 2870μm·s^{-1} experiment is used as the background, in (b) simulation III is used. (c-h) Comparison of volumetric strain profiles between (c-d) 50% - 30μm·s^{-1} experiment and Simulation I; (e-f) 50% - 1310μm·s^{-1} experiment and Simulation II; and (g-h) 50% - 2870μm·s^{-1} experiment and Simulation III. Net "shear-induced contraction" behaviour is indicated in black, and net "shear-induced dilation" is indicated in green. Profile plots with red axes correspond to the red ROI; plots with blue axes correspond to the blue ROI. Volumetric strain was measured in experiments by X-ray intensity processing (XIP), and in simulations as ($\varepsilon_{xx} + \varepsilon_{yy}$) from triangulation (TRI).
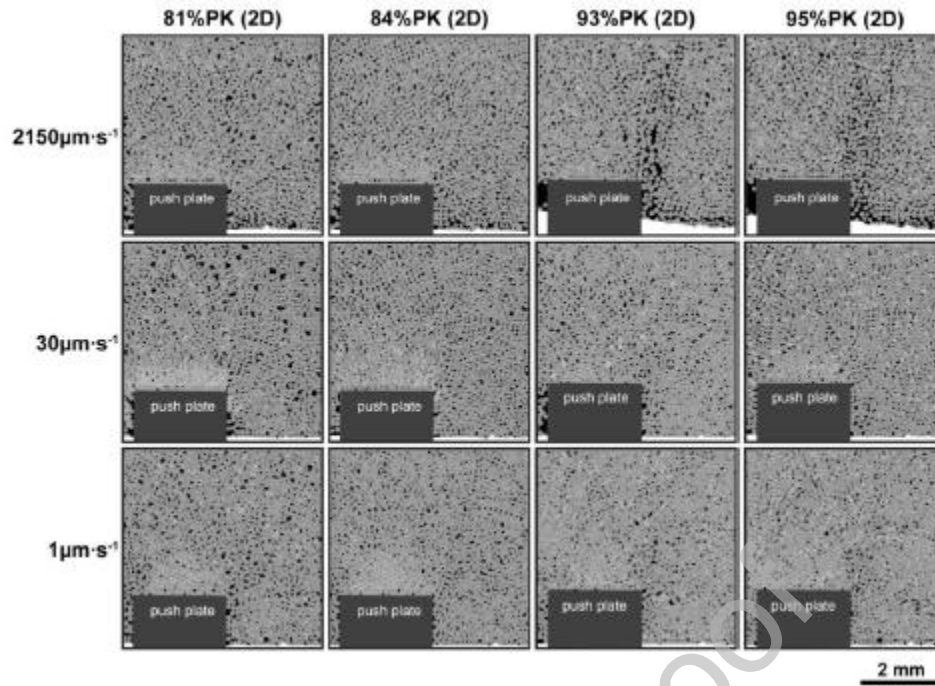
Fig. 7. Simulated deformation microstructures from LBM-DEM simulations when $u_y = 10\bar{d}$. A similar FOV to the experimental radiographs is used. The liquid-filled interstices are coloured black.
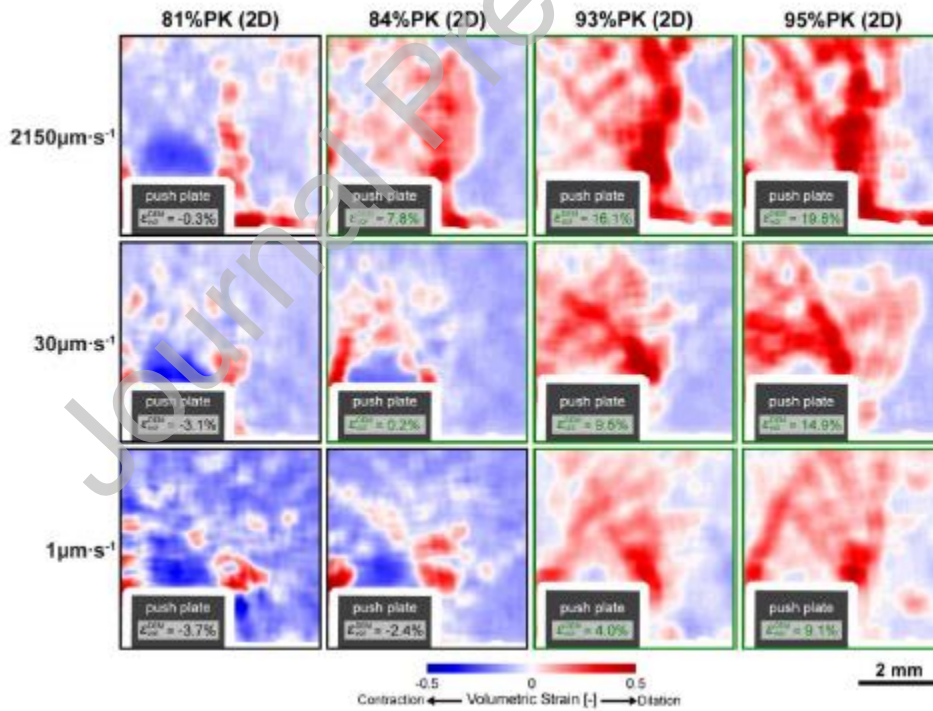

Fig. 8. Plots of volumetric strain ($\varepsilon_{xx} + \varepsilon_{yy}$) field from triangulation (averaged over a $\sqrt{10}\bar{d} \times \sqrt{10}\bar{d}$ REV) from LBM-DEM simulations when $u_y = 10\bar{d}$. The same FOV is used as in Fig. 7. $\varepsilon_{vol}^{\text{DEM}}$ denotes the total volumetric strain. The net "shear-induced contraction" ($\varepsilon_{vol}^{\text{DEM}} < 0$) simulations are outlined in black, and the net "shear-induced dilation" ($\varepsilon_{vol}^{\text{DEM}} > 0$) simulations are outlined in green.

Fig. 9. Plots of shear strain (ε_{xy}) field from triangulation (averaged over a $\sqrt{10}\bar{d} \times \sqrt{10}\bar{d}$ REV) from LBM-DEM simulations when $u_y = 10\bar{d}$. The same FOV is used as in Fig. 7. The net "shear-induced contraction" ($\varepsilon_{vol}^{DEM} < 0$) simulations are outlined in black, and the net "shear-induced dilation" ($\varepsilon_{vol}^{DEM} > 0$) simulations are outlined in green.
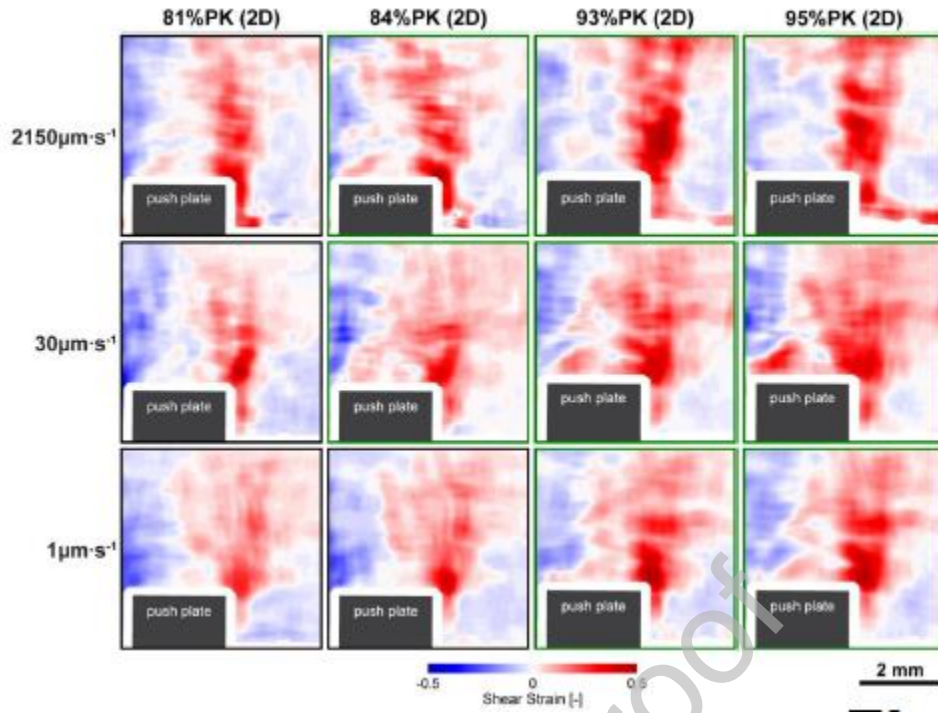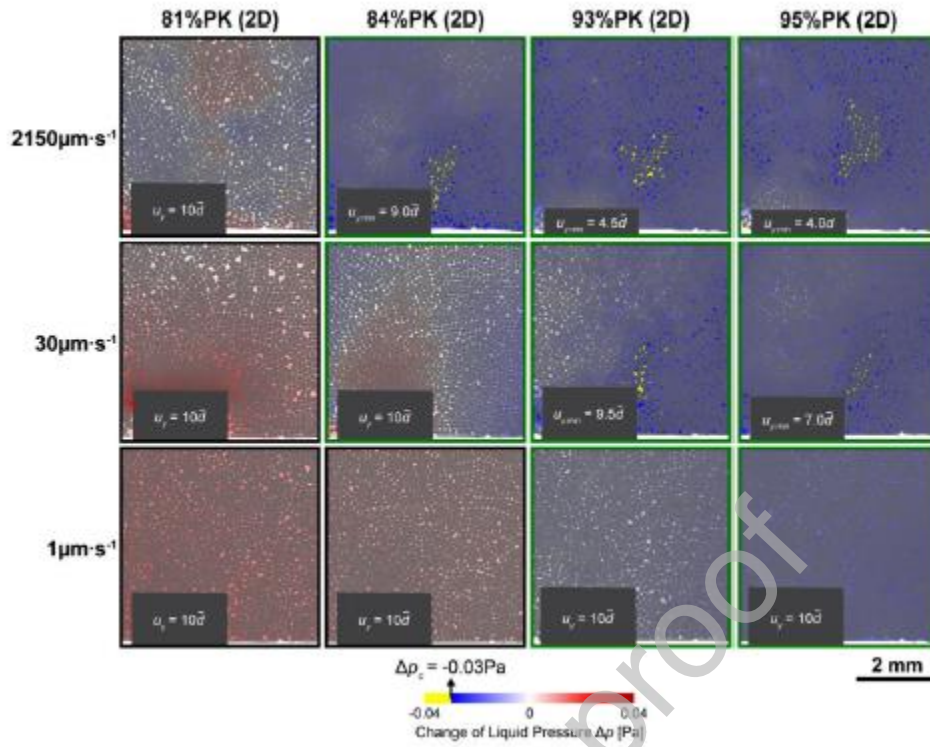
Fig. 10. Comparison liquid pressure changes as calculated in the simulations. DEM grains are coloured semi-transparent grey, and the same FOV is used as in Fig. 7. The net "shear-induced contraction" ($\varepsilon_{vol}^{\text{DEM}} < 0$) simulations are outlined in black, and the net "shear-induced dilation" ($\varepsilon_{vol}^{\text{DEM}} > 0$) simulations are outlined in green. Regions coloured yellow indicate a liquid pressure drop $\Delta p < \Delta p_c$, where $\Delta p_c = -0.03\text{Pa}$ was chosen, and $u_{y.\min}$ is the minimum normalised push-plate displacement when $\Delta p < \Delta p_c$ first occurs. For the seven simulations showing $u_y = 10\bar{d}$, no $\Delta p < \Delta p_c$ regions developed for $u_y \leq 10\bar{d}$.
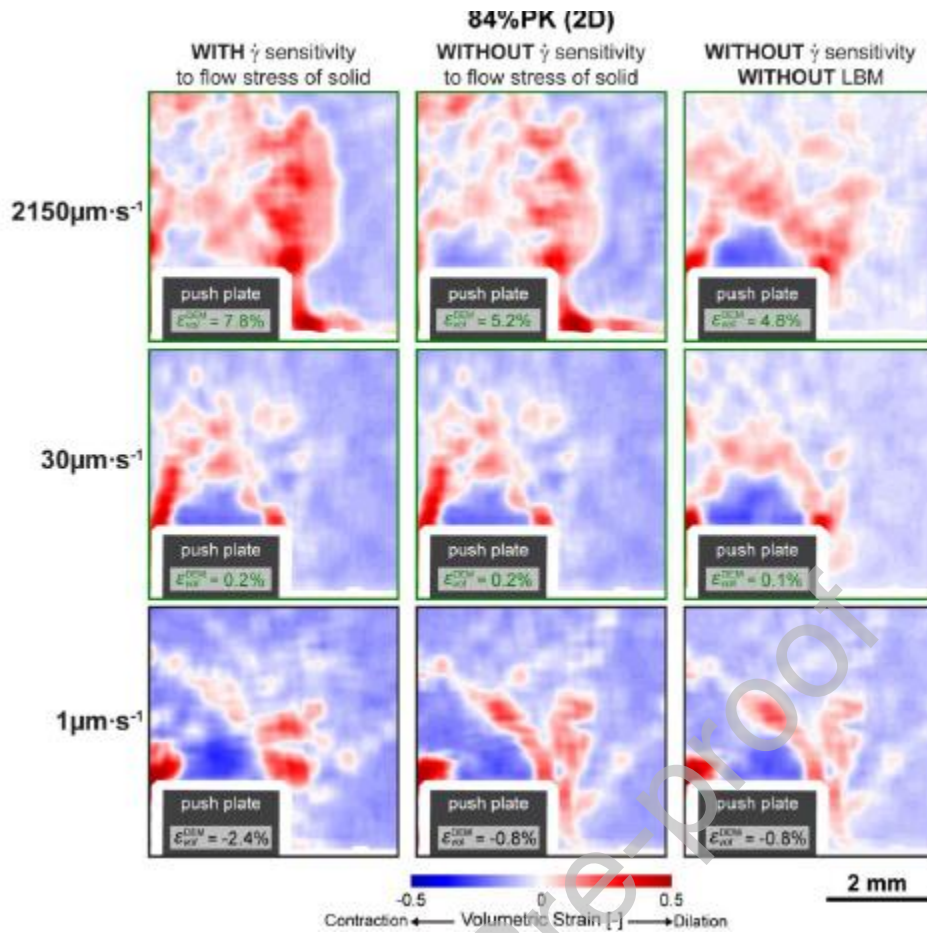
Fig. 11. Plots of volumetric strain ($\varepsilon_{xx} + \varepsilon_{yy}$) field from triangulation (averaged over $\sqrt{10}\bar{d} \times \sqrt{10}\bar{d}$ REV) for 84%PK simulations. The same FOV is used as in Fig. 7. The net "shear-induced contraction" ($\varepsilon_{vol}^{\mathrm{DEM}} < 0$) simulations are outlined in black, and the net "shear-induced dilation" ($\varepsilon_{vol}^{\mathrm{DEM}} > 0$) simulations are outlined in green. Plots in the leftmost column correspond to 84%PK simulations with strain-rate sensitivity to the flow stress of solid, followed by simulations without strain-rate sensitivity to the flow stress of solid (centre), and then simulations without strain-rate sensitivity and without interstitial liquid (i.e. no LBM) (right).
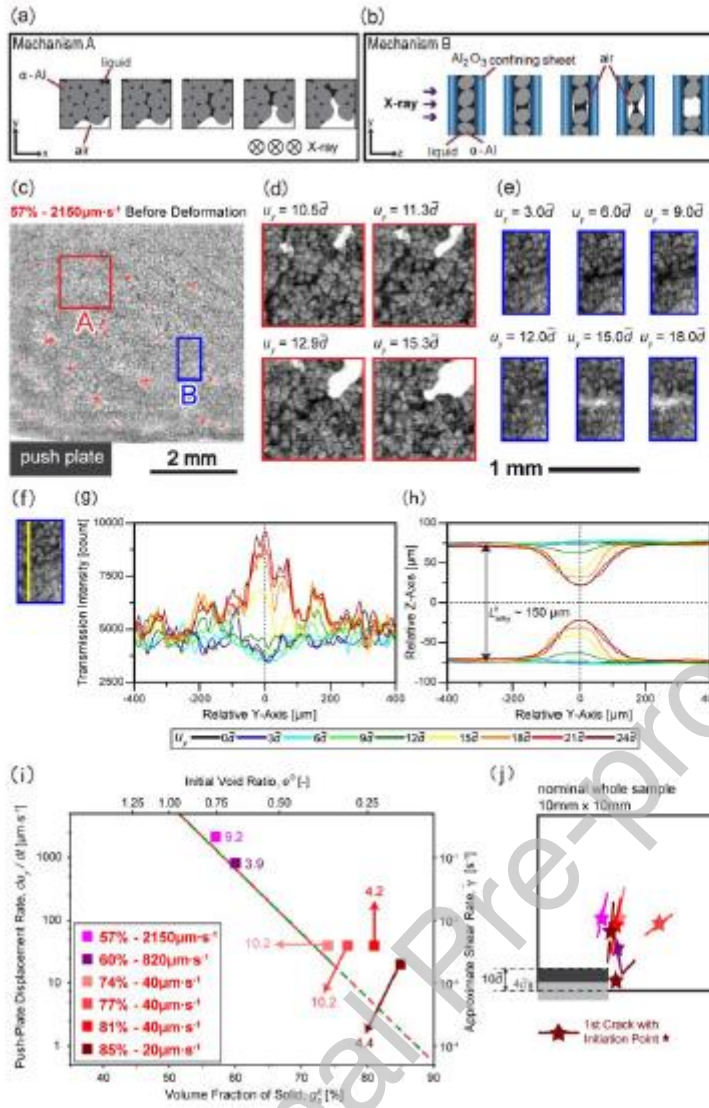
Fig. 12. (a-b) Schematic illustrations of shear cracking: (a) mechanism A, crack propagation from a free surface with a liquid meniscus in the x-y plane; (b) mechanism B, cracking from menisci in the y-z plane. (c) A radiograph of 57% - 2150μm·s^{-1} sample before deformation indicating the two regions, A and B. (d) "mechanism A" cracking in Region A, and (e) "mechanism B" cracking in Region B. (f) Yellow scanning line used to draw the profile of transmission intensity and nominal z position in Region B. (g-h) Evolution of (g) X-ray transmission intensity and (h) sample thickness along the yellow scanning line to $u_y = 24.0\bar{d}$. (i) Summary of the push-plate displacement, u_y, when the first crack formed for all six shear cracking datasets. (j) Summary of the crack positions for each dataset; the crack initiation sites are highlighted by a star.

Table 1 DEM parameters used during shear deformation stage.

| Symbol	Property	Unit	Value
ρ	Grain density	kg m^{-3}	
	81%PK Simulations		2600
	84%PK Simulations		2606
	93%PK and 95%PK Simulations		2629
	Simulation I, II, and III		2658
	Float - 0μm·s^{-1}		2634
$k_{n,e}$	Elastic normal stiffness	N m^{-1}	4×10^{-3}
$k_{n,p}$	Slope of plastic flow regime	N m^{-1}	1×10^{-7}
$k_{n,g-w}$	Grain-wall normal stiffness	N m^{-1}	31.1
$k_{n,mem}$	Membrane circle normal stiffness	N m^{-1}	0.013
$k_{n,bond}$	Mem. bonding normal stiffness	N m^{-2}	13
σ_{bond}	Tensile strength of mem. bonding	N m^{-1}	2×10^{10}
c_{bond}	Cohesion of mem. bonding	N m^{-1}	1×10^{10}
$\bar{\lambda}_{bond}$	Mem. bonding radius multiplier	−	0.5
κ	Normal-to-shear stiffness ratio	−	2.0
F_0	Avg. contact force magnitude	N	
	81%PK Simulations		2.52×10^{-9}
	84%PK Simulations		7.20×10^{-9}
	93%PK and 95%PK Simulations		4.32×10^{-8}
	Simulation I, II, and III		2.52×10^{-9}
	Float - 0μm·s^{-1}		0
U_0	Mean overlap prior to def.	m	$F_0/k_{n,e}$
F_y	Yielding contact force	N	
	1μm·s^{-1} Simulations		$F_0 + 6.6 \times 10^{-10}$
	30μm·s^{-1} Simulations		$F_0 + 1.6 \times 10^{-9}$
	Simulation II (1310μm·s^{-1})		$F_0 + 4.2 \times 10^{-9}$
	2150μm·s^{-1} Simulations		$F_0 + 4.9 \times 10^{-9}$
	Simulation III (2870μm·s^{-1})		$F_0 + 5.2 \times 10^{-9}$
	Float - 0μm·s^{-1}		$F_0 + 1.6 \times 10^{-9}$
U_y	Yielding contact overlap	N	$F_y/k_{n,e}$
F_N	Normal force on membrane	N	$0.25 \cdot F_y$
μ	Friction coefficient	−	0.05
μ_r	Rolling friction coefficient	−	0.5
Δt	Simulation timestep	s	
	1μm·s^{-1} Simulations		5.00×10^{-5}
	30μm·s^{-1} Simulations		6.66×10^{-6}
	Simulation II (1310μm·s^{-1})		1.53×10^{-7}
	2150μm·s^{-1} Simulations		9.30×10^{-8}
	Simulation III (2870μm·s^{-1})		6.97×10^{-8}
	Float - 0μm·s^{-1}		6.66×10^{-6}

Table 2 A summary for coupled LBM-DEM simulations.

Simulation dataset	Geometry adapted from experiment	# of grains, $N_{\text{grain}}^{\text{DEM}}$	Min.:avg.:max. grain size, $d_{min}^{\text{DEM}}:\bar{d}:d_{max}^{\text{DEM}}$ [μm]
81%PK - 1μm·s⁻¹	66% - 30μm·s⁻¹	5083	100:120:149
81%PK - 30μm·s⁻¹		5083	100:120:149
81%PK - 2150μm·s⁻¹		5083	100:120:149
84%PK - 1μm·s⁻¹		5224	102:120:151
84%PK - 30μm·s⁻¹		5224	102:120:151
84%PK - 2150μm·s⁻¹		5224	102:120:151
93%PK - 1μm·s⁻¹		5224	116:135:171
93%PK - 30μm·s⁻¹		5224	116:135:171
93%PK - 2150μm·s⁻¹		5224	116:135:171
95%PK - 1μm·s⁻¹		5788	116:135:171
95%PK - 30μm·s⁻¹		5788	116:135:171
95%PK - 2150μm·s⁻¹		5788	116:135:171
Simulation I	50% - 30μm·s⁻¹	7054	91:120:165
Simulation II	50% - 1310μm·s⁻¹	6019	89:120:154
Simulation III	50% - 2870μm·s⁻¹	6055	86:120:157
Float - 0μm·s⁻¹	44% - 30μm·s⁻¹ 38% - 0μm·s⁻¹	7907	057:075:094*

*The grain size in the first floating test

Table 3 Liquid parameters used in coupled LBM-DEM simulations.

Symbol	Property	Unit	Value
ρ_L	Liquid density,	kg m^{-3}	
	81%PK Simulations		2673
	84%PK Simulations		2709
	93%PK and 95%PK Simulations		2830
	Simulation I, II, and III		2948
	Float - 0μm·s^{-1}		2856
μ_L	Liquid dynamic viscosity	Pa s	
	81%PK Simulations		1.53×10^{-3}
	84%PK Simulations		1.58×10^{-3}
	93%PK and 95%PK Simulations		1.77×10^{-3}
	Simulation I, II, and III		1.99×10^{-3}
	Float - 0μm·s^{-1}		1.82×10^{-3}
δt	LBM Simulation timestep	s	
	1μm·s^{-1} Simulations		1.00×10^{-3}
	30μm·s^{-1} Simulations		6.66×10^{-4}
	Simulation II (1310μm·s^{-1})		1.53×10^{-4}
	2150μm·s^{-1} Simulations		9.30×10^{-5}
	Simulation III (2870μm·s^{-1})		6.97×10^{-5}
	Float - 0μm·s^{-1}		6.66×10^{-4}
$r_{\delta t/\Delta t}$	LBM-DEM timestep ratio	–	
	1μm·s^{-1} Simulations		20
	30μm·s^{-1} Simulations		100
	Simulation II (1310μm·s^{-1})		1000
	2150μm·s^{-1} Simulations		1000
	Simulation III (2870μm·s^{-1})		1000
	Float - 0μm·s^{-1}		100

Graphical Abstract
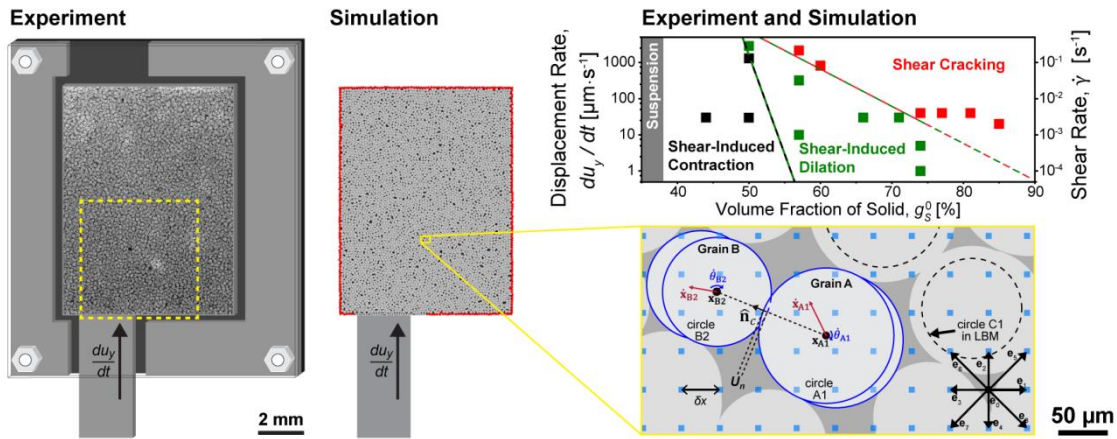
Declaration of interests

☒ The authors declare that they have no known competing financial interests or personal relationships that could have appeared to influence the work reported in this paper.

☐The authors declare the following financial interests/personal relationships which may be considered as potential competing interests: